

TOPICAL REVIEW

Optical properties and plasmons in moiré structures

To cite this article: Xueheng Kuang *et al* 2024 *J. Phys.: Condens. Matter* **36** 173001

View the [article online](#) for updates and enhancements.

You may also like

- [Klein tunneling degradation and enhanced Fabry-Pérot interference in graphene/h-BN moiré-superlattice devices](#)
Viet-Anh Tran, Viet-Hung Nguyen and Jean-Christophe Charlier
- [Moiré modulation of charge density waves](#)
Zachary A H Goodwin and Vladimir I Fal'ko
- [Moiré Dirac fermions in transition metal dichalcogenides heterobilayers](#)
Chenglong Che, , Yawei Lv et al.

Topical Review

Optical properties and plasmons in moiré structures

Xueheng Kuang¹ , Pierre A Pantaleón Peralta² , Jose Angel Silva-Guillén² ,
Shengjun Yuan^{3,4} , Francisco Guinea^{2,5}  and Zhen Zhan^{2,*} 

¹ Yangtze Delta Industrial Innovation Center of Quantum Science and Technology, Suzhou 215000, People's Republic of China

² Instituto Madrileño de Estudios Avanzados, IMDEA Nanociencia, Calle Faraday 9, 28049 Madrid, Spain

³ Key Laboratory of Artificial Micro- and Nano-structures of the Ministry of Education and School of Physics and Technology, Wuhan University, Wuhan 430072, People's Republic of China

⁴ Wuhan Institute of Quantum Technology, Wuhan 430206, People's Republic of China

⁵ Donostia International Physics Center, Paseo Manuel de Lardizábal 4, 20018 San Sebastián, Spain

E-mail: zhenzhanh@gmail.com

Received 12 September 2023, revised 26 November 2023

Accepted for publication 17 January 2024

Published 31 January 2024



CrossMark

Abstract

The discoveries of numerous exciting phenomena in twisted bilayer graphene (TBG) are stimulating significant investigations on moiré structures that possess a tunable moiré potential. Optical response can provide insights into the electronic structures and transport phenomena of non-twisted and twisted moiré structures. In this article, we review both experimental and theoretical studies of optical properties such as optical conductivity, dielectric function, non-linear optical response, and plasmons in moiré structures composed of graphene, hexagonal boron nitride (hBN), and/or transition metal dichalcogenides. Firstly, a comprehensive introduction to the widely employed methodology on optical properties is presented. After, moiré potential induced optical conductivity and plasmons in non-twisted structures are reviewed, such as single layer graphene-hBN, bilayer graphene-hBN and graphene-metal moiré heterostructures. Next, recent investigations of twist-angle dependent optical response and plasmons are addressed in twisted moiré structures. Additionally, we discuss how optical properties and plasmons could contribute to the understanding of the many-body effects and superconductivity observed in moiré structures.

Keywords: moiré structures, optical conductivity, plasmons, twisted bilayer graphene

1. Introduction

Two-dimensional (2D) materials, such as graphene [1], hexagonal boron nitride (hBN) [2, 3], transition metal dichalcogenides (TMDCs) [4, 5] and many others [6, 7], have been widely investigated over the past two decades [8]. The fact that the isolated atomic planes could be stacked

layer by layer via weak van der Waals interactions, forming moiré structures, provides an avenue to realize functionalities distinct from the components of the moiré systems [9]. Interestingly, heterostructures of two materials with different lattice constants form large-scale structures that display a moiré pattern, which we will refer to as non-twisted moiré structures. For example, by depositing graphene on top of hBN, if they are aligned, we would obtain a graphene-hBN moiré structure with a moiré length of around 14 nm [10]. Moiré structures can also be obtained by rotating two layers

* Author to whom any correspondence should be addressed.

with a relative twist angle, which are commonly known as twisted moiré structures [11, 12]. Twisted moiré structures have attracted tremendous attentions due to the emergence of a rich phase diagram of correlated states. For instance, in twisted bilayer graphene (TBG), when two graphene layers are rotated by an angle of 1.05° , known as the magic angle, flat bands appear at the charge neutrality point [13, 14]. As a consequence, exotic phenomena are observed, ranging from unconventional superconductivity [15–17] to correlated insulator phases [18–22], topological Chern insulators [23, 24], ferromagnetism [25–27], anomalous Hall effects [26, 28, 29] and non-linear Hall effects [30]. These findings have also motivated further search of electronic flat bands in other twisted moiré structures like twisted trilayer graphene (TTG) [31–33], twisted double bilayer graphene (TDBG) [34–37], twisted bilayer TMDCs [38–44], twisted bilayer hBN [45–48], and so on. In fact, correlated insulators and tunable superconductivity have also been found in twisted multilayer graphene systems [49–58]. Emergence of flat bands can also induce orbital ferromagnetism and correlated insulator states in non-twisted moiré structures such as aligned trilayer ABC graphene-hBN [59–62], and hBN-graphene-hBN heterostructures [63]. On the other hand, twisted bilayer TMDCs can also be exceptional frameworks for investigating many-body insulators [64, 65], Hubbard physics [66, 67] and the quantum anomalous Hall effect [68–71]. More importantly, large-scale moiré structures also enables exciting photonic and optoelectronic properties, like moiré excitons [72] and polaritons as, reviewed in [73]. In the search for downscaling technological devices, optical properties, such as optical conductivity [74–76], dielectric function [77–80], etc have been extensively explored in 2D materials. The unique electronic structure of graphene has motivated research focused on the fields of non-linear plasmon response [81], plasmon-polariton [82, 83], and other plasmonics [84]. From the perspective of applications, graphene stands out to be a very promising candidate for terahertz to mid-infrared applications [85], such as modulators, polarizers, mid-infrared photodetectors or mid-infrared vibrational spectroscopy [86, 87]. Furthermore, to make significant advances in the confinement of light, plasmons have been extensively studied in graphene and TMDCs and have been shown to have potential applications for the development of new state-of-the-art optical devices [86, 88–92]. From a fundamental point of view, the optical and plasmon properties of 2D materials are extremely sensitive to their band structure. Thus, the optical properties could shed light on electronic structure [93], which could serve to further investigate exotic quantum phases. Since moiré structures can exhibit distinct electronic properties from their building block counterparts, moiré structures such as TBG can lead to numerous exciting optical phenomena and could be used in future generations of optoelectronic devices [94, 95]. Here, we present an overview of the recent progress in the matter of emerging linear optical response, plasmons and their relations to other interesting properties in both non-twisted and twisted moiré structures.

This review is organized as follows: section 2 introduces the common experimental and theoretical methods for investigating optical properties and plasmons. Optical properties and plasmons are described for non-twisted moiré structures, and for twisted moiré structures in sections 3 and 4, respectively. The relation to other properties such as many-body effects and superconductivity, and a brief description of the non-linear optical response are discussed in section 5. In section 6 we give a final summary and future perspectives.

2. Methodology

This section is devoted to the introduction of the experimental techniques and theoretical framework that are needed to study the linear optical response of moiré structures.

2.1. Experimental techniques

In general, 2D materials and 2D material-based moiré structures are expected to show strong light–matter interaction and enriched photoresponses. For 2D systems, the response to an applied electromagnetic field can be mainly characterized by the optical conductivity, $\sigma(\omega)$. Since the optical conductivity is uniquely determined by the band structure, it is a powerful tool to understand the electronic properties of materials. Experimentally, infrared spectroscopy (IR) is a widely used technique to measure the optical conductivity of a material [86]. Another promising technique is the scattering-type scanning near-field optical microscope (s-SNOM) [96], which could provide the propagation of the surface plasmons by measuring the scattering amplitude $S_{\text{opt}}(x)$. The advantage of the s-SNOM is that, from the plasmon dispersion, it is possible to extract the optical conductivity $\sigma(\omega)$ and loss function $S(\mathbf{q}, \omega)$, enabling experimental access to both the electronic band structure and electron–hole excitations of the systems [97, 98]. Electron energy-loss spectroscopy (EELS) has also advanced in recent decades to provide the structural and optical characterization of materials by correlating the acquired infrared-to-ultraviolet spectral data with morphological and structural information derived from secondary electron images (in scanning electron microscope (SEM)) or the high-angle annular dark-field signal (in transmission electron microscope (TEM)) [99]. The loss function $S(\mathbf{q}, \omega)$ can be extracted from the EELS spectra. Currently, the measured results are a collection of signals from large area samples, which are unable to provide the local structure of the moiré system and could be influenced by extrinsic effects, for example, twist angle inhomogeneities or strain present in the sample. Thanks to the development of new techniques, such as 4D scanning TEM spectroscopy [100] and near-field scanning [101], it is possible to locally probe the optoelectronic properties and could be used to study the properties of moiré structures.

2.2. Theoretical methods

Concerning the theoretical approach, through linear response theory, we can obtain optical properties by calculating different response functions. For example, the optical conductivity $\sigma(\omega)$, and the polarization function $\Pi_0(\mathbf{q}, \omega)$ are evaluated from the current-current and non-interacting density–density response functions, respectively. Other optical properties such as the dielectric function $\varepsilon(\mathbf{q}, \omega)$, loss function $S(\mathbf{q}, \omega)$ and the optical absorption coefficient can be extracted from those quantities, as discussed below.

2.2.1. Linear optical response. The optical conductivity can be derived using the Kubo formula [102] and can be written as the Kubo–Greenwood equation [103]

$$\sigma_{\alpha_1\alpha_2}(\omega) = \frac{g_s i}{(2\pi)^D} \int_{\text{BZ}} d^D k \sum_{l,l'} \frac{n_F(E_{kl'}) - n_F(E_{kl})}{E_{kl} - E_{kl'}} \frac{\langle \mathbf{k}l' | J_{\alpha_1} | \mathbf{k}l \rangle \langle \mathbf{k}l | J_{\alpha_2} | \mathbf{k}l' \rangle}{E_{kl'} - E_{kl} + \hbar\omega + i\delta}, \quad (1)$$

where g_s is the spin degeneracy, D is the dimension of moiré structures and is typically set to 2 for 2D materials. J_{α_1} and J_{α_2} are current operators along the α_1 and α_2 directions, respectively. n_F is the Fermi–Dirac distribution. Eigenvalues, E_{kl} , and eigenstates, $|\mathbf{k}l\rangle$, with band index l and momentum \mathbf{k} , are needed to describe optical band transitions between l and l' bands. The integration runs over the whole Brillouin zone (BZ).

By combining the Kubo formula with the tight-binding propagation method (TBPM), the optical conductivity (omitting the Drude contribution at $\omega = 0$) could be expressed as [104, 105]

$$\sigma_{\alpha_1\alpha_2}(\omega) = \lim_{\varepsilon \rightarrow 0^+} \frac{e^{-\beta\hbar\omega} - 1}{\hbar\omega\Omega} \int_0^\infty e^{-\varepsilon t} (\sin\omega t - i\cos\omega t) \times 2\text{Im} \times \left\{ \langle \varphi | n_F(H) e^{iHt} J_{\alpha_1} e^{-iHt} [1 - n_F(H)] J_{\alpha_2} | \varphi \rangle \right\} dt, \quad (2)$$

where Ω is the area of the system, $\beta = 1/(k_B T)$ being k_B the Boltzmann constant, H is the Hamiltonian, and $|\varphi\rangle$ is the initial state of the system, which is a random superposition of all basis states

$$|\varphi\rangle = \sum_i a_i |i\rangle, \quad (3)$$

where $|i\rangle$ are all basis states in real space and a_i are random complex numbers normalized as $\sum_i |a_i|^2 = 1$.

The calculation of equation (2) scales linearly with the number of states N of the system in real space. In contrast, the scaling would be $O(N^3)$ if we were to solve equation (1) using the exact diagonalization method to obtain the eigenstates and eigenvalues of the system. Therefore, calculating the optical conductivity using equation (2) has advantages when dealing with non-periodic moiré structures, such as 30° dodecagonal graphene quasicrystal [106–110] and large-scale periodic moiré structures [105]. Interestingly, disorder effects on

optical conductivity can be also easily be considered with this real-space method [111]. It is important to note that there are similar real-space methods with $O(N)$ time scaling that do not require time propagation to calculate transport conductivity $\sigma_{\alpha\beta}(\omega = 0)$ [112, 113].

The optical conductivity corresponds to the optical absorption spectrum that can be extracted from raw data of IR using multilayer Kramers–Kronig analysis program [114], and is related to the transmission of incident light perpendicular to the system, which is given by [115]

$$T = \left| 1 + \frac{2\pi}{c} \sigma(\omega) \right|^{-2} \approx 1 - \frac{4\pi}{c} \text{Re} \{ \sigma(\omega) \}. \quad (4)$$

Absorbance at normal incidence could be expressed as [75]

$$A = \frac{4\pi}{c} \text{Re} \{ \sigma(\omega) \}, \quad (5)$$

where $\text{Re} \{ \sigma(\omega) \}$ is the real part of optical conductivity.

2.2.2. Polarization function. The polarization function, Π_0 , also known as charge susceptibility or non-interacting density–density response function, describes the charge fluctuation or single-particle transitions. Therefore, it is imperative to further describe collective excitations and screening in materials. For small-scale systems, such as large-angle twisted moiré structures whose eigenstates and eigenvalues can be obtained by diagonalization of the Hamiltonian, the polarization function can be solved by using the Lindhard function [116–118]

$$\Pi_0(\mathbf{q}, \omega) = \frac{g_s}{(2\pi)^2} \int_{\text{BZ}} d^2 \mathbf{k} \sum_{l,l'} \frac{n_F(E_{\mathbf{k}'l'}) - n_F(E_{\mathbf{k}l})}{E_{\mathbf{k}'l'} - E_{\mathbf{k}l} - \omega - i\delta} \times |\langle \mathbf{k}'l' | e^{i\mathbf{q}\cdot\mathbf{r}} | \mathbf{k}l \rangle|^2, \quad (6)$$

where $\mathbf{k}' = \mathbf{k} + \mathbf{q}$, $\delta \rightarrow 0^+$. Generally, the integral is taken over the whole BZ, same as in equation (1). Note here that we named the polarization function without many-body effects and local field effects (LFEs) as $\Pi_0(\mathbf{q}, \omega)$.

Combining the TBPM with the Kubo formula, the polarization function can also be described as [105, 119]

$$\Pi_0(\mathbf{q}, \omega) = -\frac{2}{\Omega} \int_0^\infty dt e^{i\omega t} \text{Im} \langle \varphi | n_F(H) e^{iHt} \rho(\mathbf{q}) e^{-iHt} \times [1 - n_F(H)] \rho(-\mathbf{q}) | \varphi \rangle, \quad (7)$$

in which $\rho(\mathbf{q}) = \sum_i c_i^\dagger c_i \exp(i\mathbf{q} \cdot \mathbf{r}_i)$ is the density operator, \mathbf{r}_i is the position of the i th orbital and Ω is the area of a moiré structure system, $|\varphi\rangle$ has the same form as equation (3). Equation (7) is equivalent to the Lindhard function (equation (6)), which has been widely used in the study of single-layer graphene and TBG [120]. The Lindhard function has the advantage that it can be used to study specific attributions of band transitions, such as the intraband and interband contributions to the polarization function in moiré structures, while this information cannot be extracted from equation (7). However, when the full-band contribution to the polarization

function is required to investigate screening effects in moiré structures, equation (7) will be a reliable choice with lower computational complexity in comparison to the calculation of the Lindhard function (6) since it includes all possible electronic excitations in moiré structures. More details related to the TBPM and equation (7) are discussed in [105].

2.2.3. Dielectric function and plasmons. The dielectric function can be derived from the polarization function, $\Pi_0(\mathbf{q}, \omega)$, or the optical conductivity $\sigma(\omega)$. In the random phase approximation (RPA), the dielectric function relates directly to $\Pi_0(\mathbf{q}, \omega)$ as

$$\varepsilon(\mathbf{q}, \omega) = 1 - V(q)\Pi_0(\mathbf{q}, \omega), \quad (8)$$

where $V(q)$ is the Fourier component of the Coulomb interaction. For example, the pure 2D Coulomb interaction is $V(q) = 2\pi e^2/(\varepsilon_B q)$ with ε_B the background dielectric constant. Specifically, in the long wavelength limit $\mathbf{q} \rightarrow 0$, the RPA dielectric function is linked to $\sigma(\omega)$ as [121]

$$\varepsilon(\mathbf{q}, \omega) = 1 + \frac{iq^2 V(q)}{\omega} \sigma(\omega). \quad (9)$$

Note that the accuracy of equation (9) is lower when q gets larger due to the local approximation used in the optical conductivity, but equation (8) is valid even for large q because the polarization function is not a local property and dependent on q , whereas the optical conductivity $\sigma(\omega)$ is independent on q . The internal electronic screening potential can be given by the dielectric function as [122]

$$V_{\text{scr}}(\mathbf{q}, \omega) = \frac{V(q)}{\varepsilon(\mathbf{q}, \omega)}. \quad (10)$$

A plasmon mode with momentum \mathbf{q} and frequency ω_p can be obtained from the dielectric function with $\varepsilon(\mathbf{q}, \omega) = 0$ [122]. The plasmon mode can be also measured from the electron energy loss function

$$S(\mathbf{q}, \omega) = -\text{Im} \frac{1}{\varepsilon(\mathbf{q}, \omega)}, \quad (11)$$

with a sharp pole when $\omega = \omega_p$. The loss function is closely related to results obtained with EELS in experiments since the peaks in the data are related to the energy of the plasmon modes. Besides the experimental quantities of $\sigma_{\alpha\beta}(\omega)$ and $S(\mathbf{q}, \omega)$ that can be directly reproduced by the numerical calculations, these optical quantities could shed light on calculated electronic structures, for example, the bandwidth, band gap and Fermi velocity and so on, which is a good starting point to further understand exotic quantum phases.

Here, it should be noted that the limitation of RPA when the charge density is small and dimension of moiré structures is low, since vertex corrections could not be safely ignored in the dielectric function calculation [123]. Based on many-body perturbation theory, the effects of vertex corrections on the dielectric function can be evaluated by taking into account the interaction between two non-interacting Green functions

[124–126], which are employed to derive the non-interacting density–density response function equation (6). Actually, previous studies have shown that vertex corrections has an impact on polarization function and plasmons in both doped and undoped graphene [125–127]. Beyond RPA, the exchange–correlation (EX) effects also play a role in affecting the dielectric function and plasmons [128]. But, the EX effects can be incorporated into the RPA scheme using local-field corrections, which could be formulated by a dielectric function with a local-field factor that cannot be determined by a self-consistent calculation [129–132].

2.2.4. LFEs. When confronted with inhomogeneous electron systems, it is crucial to consider the LFEs [133, 134], via an Umklapp process in the analysis of optical properties and plasmons [135–137]. The LFEs become stronger as the momentum transfer q increases, since then the wavelength of the excitation becomes smaller and one has to take the inhomogeneities of the electronic system under consideration. For example, for a moiré structure with large moiré length and/or large wavenumber q , when the investigated q becomes comparable to the length of the first reciprocal moiré lattice vector, the LFE could significantly change the plasmon properties. The polarization function of including the LFE is given by

$$\begin{aligned} \Pi_{\mathbf{G}, \mathbf{G}'}(\mathbf{q}, \omega) &= \frac{g_s}{(2\pi)^2} \int_{\text{BZ}} d^2\mathbf{k} \sum_{l, l'} \frac{n_F(E_{\mathbf{k}'l'}) - n_F(E_{\mathbf{k}l})}{E_{\mathbf{k}'l'} - E_{\mathbf{k}l} - \omega - i\delta} \\ &\times \langle \mathbf{k}l | e^{-i(\mathbf{q}+\mathbf{G})\cdot\mathbf{r}} | \mathbf{k}'l' \rangle \langle \mathbf{k}'l' | e^{i(\mathbf{q}+\mathbf{G}')\cdot\mathbf{r}} | \mathbf{k}l \rangle, \end{aligned} \quad (12)$$

where \mathbf{G} and \mathbf{G}' are arbitrary reciprocal lattice vectors. The dielectric function within LFE is given by the following matrix under RPA

$$\varepsilon_{\mathbf{G}, \mathbf{G}'}(\mathbf{q}, \omega) = \delta_{\mathbf{G}, \mathbf{G}'} - V(\mathbf{q} + \mathbf{G})\Pi_{\mathbf{G}, \mathbf{G}'}(\mathbf{q}, \omega), \quad (13)$$

with the 2D Coulomb potential $V(\mathbf{q} + \mathbf{G}) = 2\pi e^2/\varepsilon_B(\mathbf{q} + \mathbf{G})$. The off-diagonal matrix elements in equation (13) give rise to LFE. If $G = G' = 0$, the dielectric matrix equation (13) reduces to the Lindhard dielectric function in equation (8). The optically detected macroscopic dielectric function is given by [133, 134]

$$\varepsilon_M(\mathbf{q}, \omega) = \frac{1}{\varepsilon_{G=0, G'=0}^{-1}(\mathbf{q}, \omega)}, \quad (14)$$

where ε^{-1} is the inverse of the matrix $\varepsilon_{\mathbf{G}, \mathbf{G}'}$. By comparing the macroscopic dielectric function $\varepsilon_M(\mathbf{q}, \omega)$ to equation (8), one can know how LFE affect optical properties in a crystal [135]. The energy loss function is formulated as $S(\mathbf{q}, \omega) = -\text{Im}(\frac{1}{\varepsilon_M(\mathbf{q}, \omega)}) = -\text{Im}[\varepsilon]_{G=0, G'=0}^{-1}(\mathbf{q}, \omega)$.

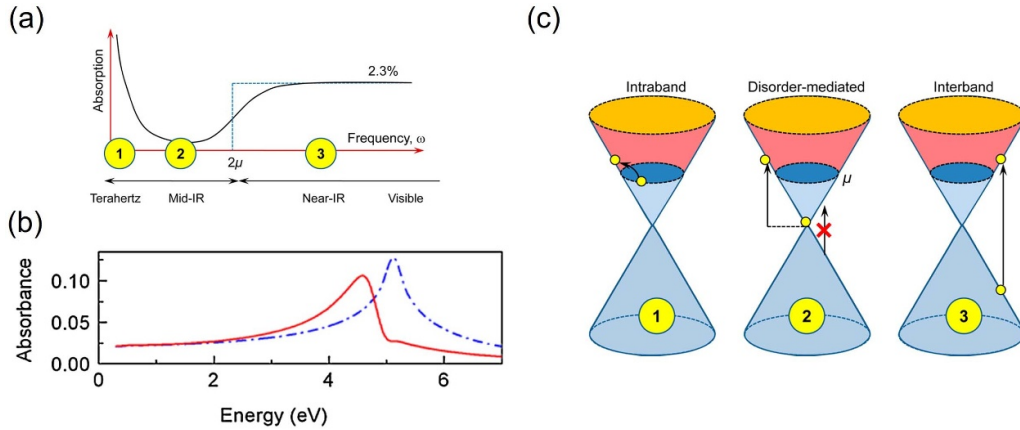


Figure 1. Optical conductivity in monolayer graphene. (a) Illustration of a typical absorption spectrum of doped graphene. Reprinted with permission from [86]. Copyright (2014) American Chemical Society. (b) First-principles absorbance of graphene with (red line) and without (blue line) excitonic effects included. Reprinted (figure) with permission from [138], Copyright (2009) by the American Physical Society. (c) Illustration of the various optical transition processes. Reprinted with permission from [86]. Copyright (2014) American Chemical Society.

3. Optical properties and plasmons in non-twisted moiré structures

3.1. Optical conductivity in graphene-based moiré structures

The optical properties of the graphene monolayer have many intriguing features [82–84], such as a constant optical conductivity in the infrared regime and gate-dependent optical absorbance [86]. As shown in figure 1, firstly, there is a Drude peak at terahertz (THz) frequencies due to the intraband transitions. Secondly, for graphene with doping μ , a minimal absorption in the mid-infrared frequencies occurs at finite $\omega < 2\mu$ due to Pauli blocking. Thirdly, a transition occurs around $\omega \approx 2\mu$ where direct interband processes lead to a constant optical conductivity $\sigma_0 = \pi e^2/2h$. Finally, a sharp peak is located at $2t$ (with t the intralayer nearest neighbor hopping in graphene) arising from the interband transitions between the two van Hove singularities (VHS), which are logarithmically divergent points in electronic density of states (DOS) and corresponding to saddle points of band structure. This peak becomes red-shifted with a different line shape if we consider the electron–hole interaction [138].

Graphene is usually supported on top of a hBN substrate to retain a high quality. When graphene is placed on the hBN substrate, a moiré pattern of 14 nm is formed in aligned samples due to the 1.8% lattice mismatch between these two 2D materials [139–141]. Undoubtedly, the periodic moiré potential induced in the graphene-hBN structure changes significantly the electronic structure of graphene and leads to various novel quantum phenomena such as the emergence of the second-generation Dirac cones (located around some moiré energy E_M), the renormalization of the Fermi velocity, and a gap opening in the intrinsic Dirac cone [141].

In the graphene-hBN moiré structure, there is a fast sublattice oscillation due to boron and nitrogen sites which results in a series of periodic potentials acting on the graphene monolayer [142]. The first one is a scalar potential, which

results from the moiré variation of the onsite terms, the second is a mass term originated from a local variation of the boron and nitrogen onsite terms, and a third one is a gauge potential resulting from the relaxation of the graphene atomic positions due to the presence of the hBN substrate [142, 143]. The resulting potentials, coupled to the electron pseudospin, can be probed directly through infrared spectroscopy, because optical transitions are very sensitive to wave functions of excited states. Consequently, in the experiment in [142], a remarkable absorption peak was detected around $2E_M \sim 380$ meV, which was only observed in the graphene-hBN heterostructure. Moreover, the absorption peaks were found to be very sensitive to electron doping, which was revealed by a sharp decrease in its weight while increasing the electron concentration [142]. The sharp drop could not be explained by the single-particle Pauli blocking effect whose energy was found to be small, but was due to a renormalization of the effective potential parameters induced by electron–electron interactions.

On the other hand, it is well-known that optical conductivity is typically dominated by the intraband Drude peak and interband transitions associated with singularities in the DOS. Theoretical works can provide a better understanding of which transitions among Bloch bands contribute to the optical conductivity. For instance, DaSilva [145] employed a $\mathbf{k}\cdot\mathbf{p}$ continuum Dirac model and the Kubo formula to investigate the optical conductivity of graphene aligned with hBN (as shown in figure 2(a)). They discovered that the moiré pattern induced sharp THz peaks due to transitions between Bloch bands formed by the moiré potential. The particle-hole asymmetry of the moiré Bloch bands (see figure 2(b)) was strongly reflected in the THz and IR conductivity, which was always Drude-dominated when the Fermi level lied above the Dirac point, but it was interband-dominated when the Fermi energy lies in a relatively narrow interval below the Dirac point. In addition, Abergel and Mucha-Kruczyński [146] suggested that a study of the absorption spectra as a function of the doping

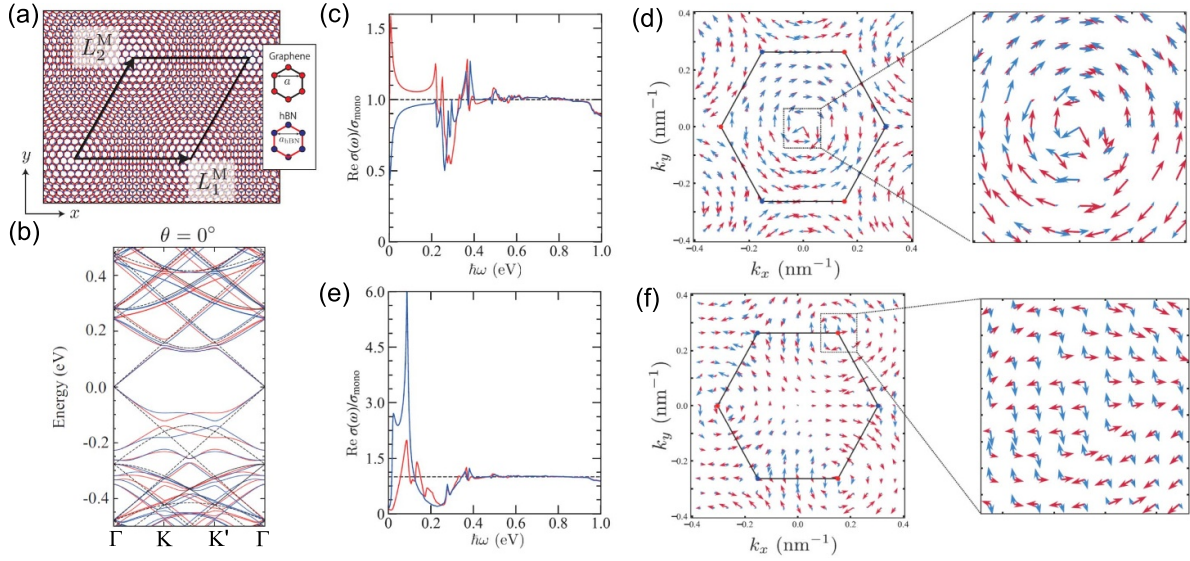


Figure 2. Valley polarization of graphene-hBN structure under circularly polarized light irradiation. (a) Crystal structure of graphene-hBN structure in real space for alignment case. (b) The band structure of graphene-hBN in the continuum model. (c) Optical conductivity of graphene-hBN for K valley and Fermi level $E_F = 0$ eV under circularly polarized light. The magenta (cyan) curve is the conductivity for LCP (RCP). (d) Distribution of dipole vectors for an interband transition near the $E_F = 0.0$ eV in momentum space. The magenta (cyan) arrows are the real (imaginary) parts of the dipole vectors. The black hexagon is the moiré BZ and the magenta (cyan) dots at the hexagon corners are the K (K') points. (e) The optical conductivity and (f) distribution of dipole vectors for $E_F = -0.13$ eV. Reprinted (figure) with permission from [144], Copyright (2022) by the American Physical Society.

for an almost completely full first miniband was necessary to extract meaningful information about the moiré characteristics from optical absorption measurements as well as to distinguish between various theoretical proposals for the physically realistic interactions between graphene and hBN. One of the main findings on [146] was the fact that distinct moiré perturbations can result in similar absorption spectra.

The effect of polarized light was studied in [144]. It was found that a broken spatial symmetry in the graphene-hBN structure may induce valley polarization, which could be investigated by measuring the optical conductivity under circularly polarized light irradiation, as shown in figures 2(c) and (e). The conductivity depended on the direction of rotation of the circularly polarized light, especially in the infrared and terahertz regions. In particular, for a photon energy smaller than 0.1 eV, the difference between left-handed circularly polarized light (LCP) and right-handed circularly polarized light (RCP) became larger. In this energy region, the interband transition from valence to conduction bands dominated. The real and imaginary parts of the dipole vectors are orthogonal at the Γ point. Thus, the valley-selective circular dichroism (valley polarization) was induced by the irradiation of circularly polarized light, and was responsible for the states near the Γ point (figure 2(d)). For hole doping case, in the region of $\omega < 0.1$ eV, the difference in the optical conductivities between LCP and RCP became larger. The real and imaginary parts of the dipole vectors are mutually orthogonal at the K and K' points, which were responsible for the valley-selective circular dichroism. In fact, the moiré potential of aligned graphene-hBN structures can be tuned by a twist

angle that continuously change optical intraband and interband transitions in graphene-hBN moiré structures [147].

3.2. Plasmons in graphene-based moiré structures

The plasmons in graphene-based heterostructures [10] have attracted a lot of attentions due to the fact that plasmons in pristine graphene have very promising perspectives [148, 149]. In this section, we will mainly review plasmonic properties in graphene-hBN and graphene-metal moiré structures.

As mentioned in section 3.1, stacking graphene on a hBN substrate allows to engineer the electronic band structure of graphene by the induced moiré potential. An important consequence is the emergence of satellite Dirac points in the moiré minibands [153] since they could give rise to collective excitations that are different from pristine graphene. In 2014, a theoretical study on plasmons in graphene-hBN unveiled that new plasmon modes can be generated due to transitions between satellite Dirac points, as shown in figure 3(a) [150]. The K-point and M-point plasmon modes (dotted and short-dashed lines in figure 3(a), respectively), appeared alongside a Dirac plasmon mode (long-dashed line) in hole-doped graphene. Based on a continuum model and including the LFE, further calculations demonstrated a dramatic asymmetry of the plasmon dispersion at positive and negative potentials, as seen in figure 3(b), and also predicted several plasmon modes arising from interband transitions between minibands. Experimentally, the measured optical response using a s-SNOM tip in moiré-patterned graphene was enhanced with

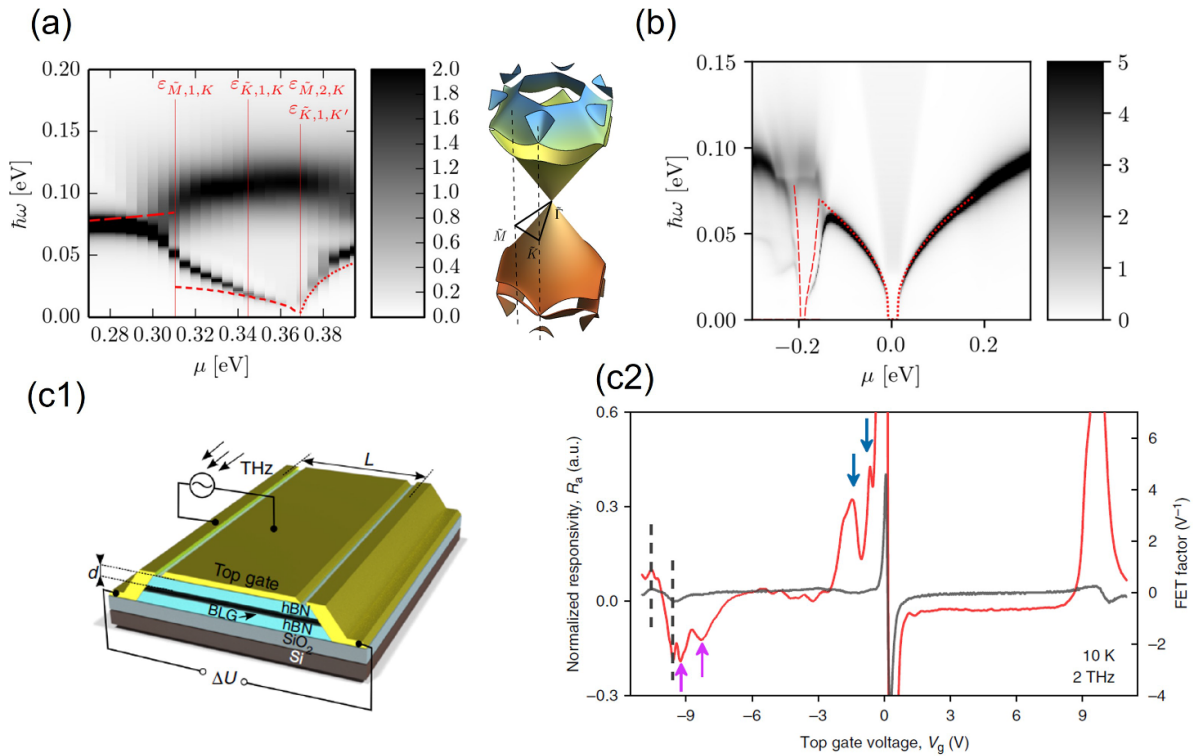


Figure 3. Plasmon in graphene-hBN moiré structures. (a) Theoretical predicted plasmon energy relation versus hole-side chemical potential in a density plot of loss function within LFE (left-hand side) and corresponding miniband structure of graphene-hBN (right-hand side). The vertical thin solid lines in the density plot denote the doping levels crossing different band edges in the miniband structure. Reprinted (figure) with permission from [150], Copyright (2014) by the American Physical Society. (b) Particle-hole asymmetric plasmon emerging in a density plot of loss function within LFE for graphene-hBN moiré structure. Reprinted (figure) with permission from [151], Copyright (2019) by the American Physical Society. (c1) Illustration of the encapsulated bilayer graphene-hBN field effect transistor. Reproduced from [152]. CC BY 4.0. (c2) Plasmons from miniband transition in bilayer graphene-hBN structure. Reproduced from [152]. CC BY 4.0.

respect to pristine graphene [97]. A composite plasmon in graphene-hBN moiré structures was also observed, originating from intraband transitions near the Fermi energy and predicted interband transitions corresponding to structure minibands [97]. Nevertheless, up to date, the calculated terahertz plasmon from [150] and asymmetry plasmon from [151] have not been observed experimentally. In addition, based on an antenna-mediated coupling of a bilayer graphene (BLG) field-effect transistor device, shown in figure 3(c1), miniband plasmons in BLG-hBN were also observed (see figure 3(c2)).

The observation of miniband plasmons in graphene-hBN also motivated the exploration of electronic excitations in graphene-metal structures. The moiré potential was induced when Cu atoms were deposited on graphene, forming a moiré structure, giving rise to extra VHS associated with minibands (see figure 4(b)). This resulted in a moiré plasmon mode with energy ~ 1.5 eV, which was contributed by interband transition between VHS (as shown in figure 4(a)). The existence of this plasmon mode was theoretically confirmed by using the TBPM method [154]. Interestingly, when the moiré potential induced in chemically doped graphene on the Ir(111) metallic surface was suppressed, plasmon could be still significantly modified, generating an acoustic plasmon (AP) mode along with an intraband Dirac plasmon (DP) mode (see figure 4(c)) [155]. This AP was induced by the screening effect of metallic materials or graphene-metal hybridization rather than by the

moiré reconstruction and had also been widely studied in previous works [156–158].

4. Optical properties and plasmons in twisted moiré structures

4.1. Optical conductivity of TBG

The recent discovery of correlated electronic states and superconductivity in TBG [12, 15, 51] has sparked a great interest in twisted moiré systems. In TBG the interlayer interactions induce significant distortions in the low-energy bands. This leads to distinctive electronic effects that differ from those observed in non-twisted graphene systems. At low angle, the interference between the moiré periods produces a long wavelength moiré pattern [14, 159–164]. Characteristic properties like VHS and band gaps become evident in the infrared region [115] and theoretical works [14, 159–165] have demonstrated that the moiré patterns in TBG can give rise to narrow bands that largely contribute to the correlated effects observed in this system [15–17, 23, 24, 51, 62, 166–179].

An interesting feature of TBG is that the VHS can be moved to arbitrary low energies by modifying the twist angle. One interesting optical analysis of TBG was performed by Yu *et al* [180]. In the experiment, different optical conductivities were obtained by varying the twist angle. As shown in

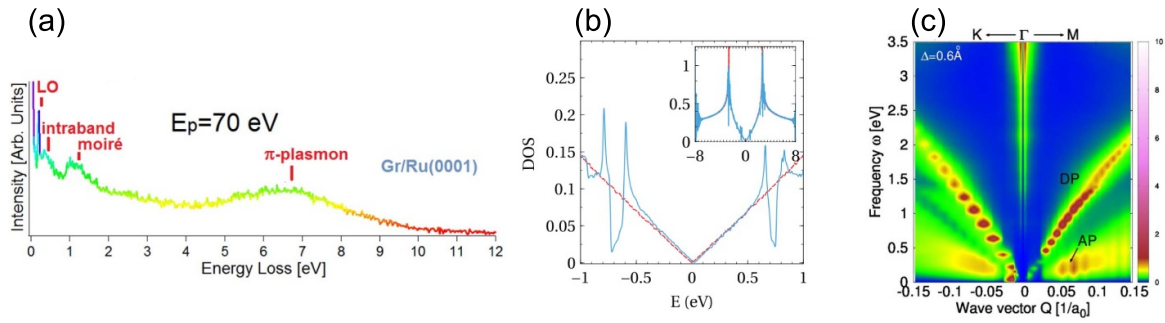


Figure 4. Plasmon in graphene-metal moiré structures. (a) High-resolution electron energy loss spectroscopy of graphene on Ru(0001), acquired with an energy of the primary electron beam E_p of 70 eV. The longitudinal optical (LO) phonon, intraband plasmon, moiré plasmon and π -plasmon are observed. Reproduced from [154]. © IOP Publishing Ltd. All rights reserved. (b) Moiré VHS in graphene-Cu moiré structures from density functional theory calculations. Reproduced from [154]. © IOP Publishing Ltd. All rights reserved. (c) The loss function intensity plot showing an acoustic plasmon (AP) predicted in graphene-metal structure doped with alkali-metal atoms. Reprinted (figure) with permission from [155]. Copyright (2019) by the American Physical Society.

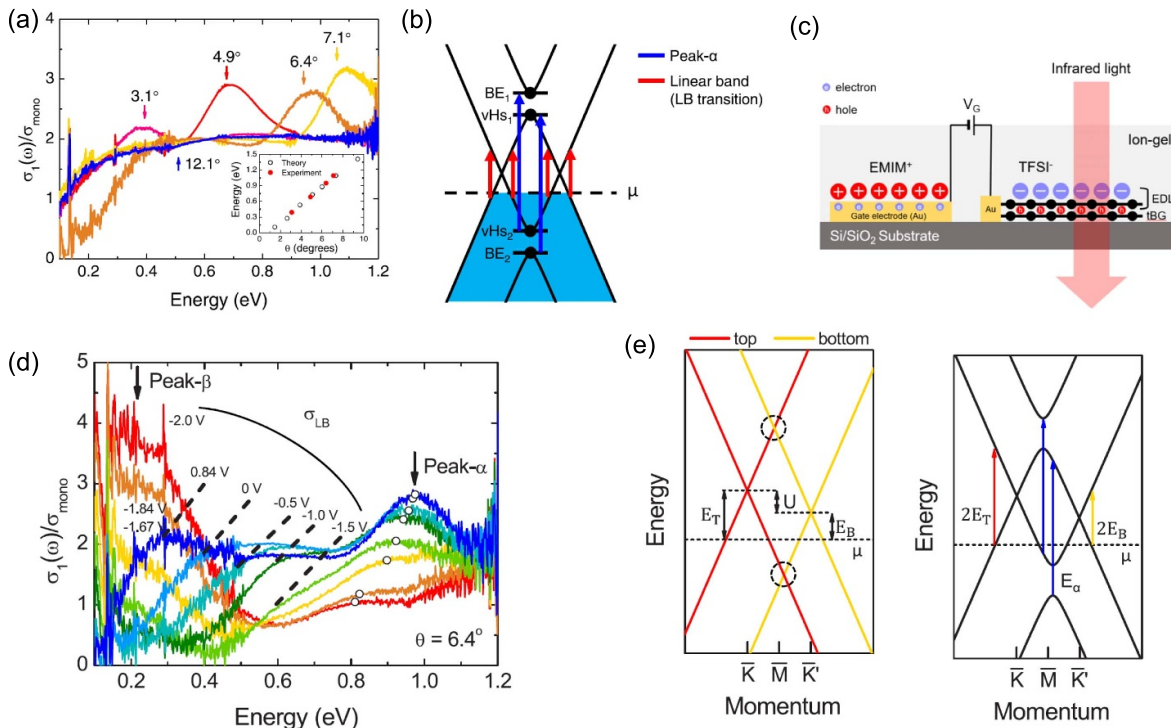


Figure 5. Gate tunable optical absorption of TBG. (a) Optical conductivity σ_1 of five TBG samples with five different twist angles. σ_{mono} is the optical conductivity of monolayer graphene. (b) Electronic band diagram of TBG. BE and vHS stand for the band edge of the second band and the saddle-point van Hove singularity, respectively. There exist two kinds of optical transitions as indicated by the red and blue arrows. (c) Schematic view of the ion-gel gating circuit and the infrared transmission measurement. EMIM and TFSI are ionic liquids. (d) Optical conductivity of TBG with various gate voltages V_G . The twist angle is $\theta = 6.4^\circ$. (e) (Left side) The band structure of TBG under gating. The top band and bottom band shift by E_T and E_B , respectively. $U = E_T - E_B$ is their difference. Here, the gap opening is omitted for clarity. (Right side) Optical transitions of the gated TBG. Reprinted (figure) with permission from [180], Copyright (2019) by the American Physical Society.

figure 5(b), the low-energy optical spectrum of TBG was characterized by a linear-band (LB) absorption (pointed out by the red arrows). This was an indication that the interlayer interaction hybridized the LBs of the two monolayers and, as a consequence, there were two isolated bands with an avoided crossing with the remote bands. In figure 5(b), the transition between the saddle-point $\text{VHS}_2 \rightarrow \text{VHS}_1$ was forbidden by the lattice symmetry [115]. However, the transition between VHS

and the band edge (BE) of the second band exhibited prominent peaks (peak- α indicated by the blue arrows). Two interesting features, shown in figure 5(a), were found in this experiment: firstly, a frequency-independent conductivity, $2\sigma_0$, which came from the LB transition, and secondly, an angle-dependent peak- α resulting from the transitions between VHSs and BE. Interestingly, the peak- α was blueshifted as the twist angle θ increased, revealing a dependence on the

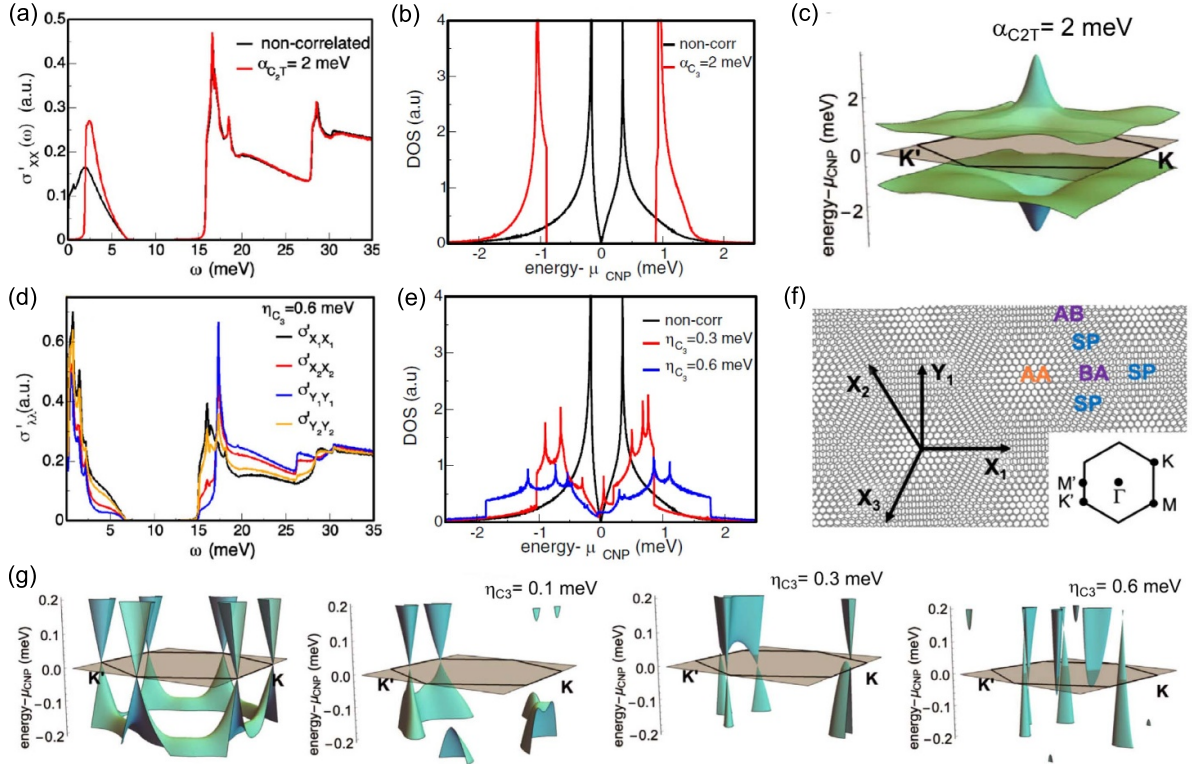


Figure 6. Optical conductivity, DOS and band structures of undoped TBG with different symmetry breaking orders. (a) Optical conductivity, and (b) low energy DOS of the TBG at the CNP in a C_2T symmetry breaking state α and in the non-correlated state. (c) Flat bands of the TBG in the C_2T symmetry breaking state. (d) Optical conductivity and (e) DOS for the nematic state η . The optical conductivity in (d) is plotted along four different directions, illustrated in (f). (f) Sketch of the C_3 related X_i directions and of Y_1 , and the BZ of TBG with the corresponding symmetry points. (g) Zoom of the flat band structure for the TBG with different values of η_{C_3} . Note that the optical conductivity in (a) along the four directions are equal. Reproduced from [185]. CC BY 4.0.

twist angle. Furthermore, by designing an ion-gel gating circuit (in figure 5(c)) it was possible to investigate the gating effect on the properties of these devices. It was found that in the absorption profile, cf figure 5(d) the absorption edge of σ_{LB} had a broadening and was shifted to higher energy, and (ii) the peak- α was shifted to a lower energy with a reduced intensity. In addition, a modification of the band structure with gating was found, because in the presence of a vertical electric field, figure 5(e), the Dirac cones of each monolayer shifted in opposite directions. This was theoretically described in [181] and recently in [182], allowing to modify the optical transitions [183].

Additional evidence of the existence of isolated narrow bands with an enhanced DOS was reported in 2013 by Zou *et al* [184]. By means of a terahertz time-domain spectroscopy, the optical conductivity of TBG was obtained at different temperatures in the frequency range 0.3–3 THz. One of the main findings in this work was a Drude-like response with a strong peak in the real part of the optical conductivity $\sigma_1(\omega)$ at ~ 2.7 THz, which was identified as peak- α (figure 5(d)) in TBG with $\theta = 1.16^\circ$, and was caused by the presence of the VHS in the commensurate structure.

Interestingly, TBG shows an angle-dependent optical conductivity, which could be utilized to characterize the twist angle. For example, Sunku *et al* [93] combined

nano-photocurrent and infrared nanoscopy methods, which enabled access to the local electronic phenomena at length scales as short as 20 nm, and identified domains of varying local twist angles. In addition, Calderón and Bascones [185] reported that the optical conductivity measurements could be used to distinguish different symmetry breaking states, and may reveal the nature of the correlated states in the flat bands that appear in TBG. As shown in figures 6(a)–(c), in a correlated order which breaks the C_2T symmetry, named α here, a gap was opened at the Dirac points in K , resulting in a reorganization of the spectral weight. In TBG without correlations or external symmetry breaking, the lattice had C_3 symmetry, figure 6(f). Moreover, in a system with C_3 symmetry $\sigma_{X_i X_j} = \sigma_{Y_i Y_j}$. Here, X_i is the direction, as illustrated in figure 6(f). Therefore, the optical conductivity along the four directions ($X_1 X_1$, $X_2 X_2$, $Y_1 Y_1$ and $Y_2 Y_2$) were equal in the correlated order, but different in the reported nematic state (named η_{C_3} , which lowers the rotational symmetry of TBG). Furthermore, in the nematic state, when the flat band was partially filled, the DOS was modified. With larger values of the amplitude of the order parameter η_{C_3} , the Dirac points moved away from the charge neutrality point and hole and electron Fermi pockets were generated. Additional Fermi pockets appeared, leading to new band crossings between the lower and upper flat bands (figure 6(g)).

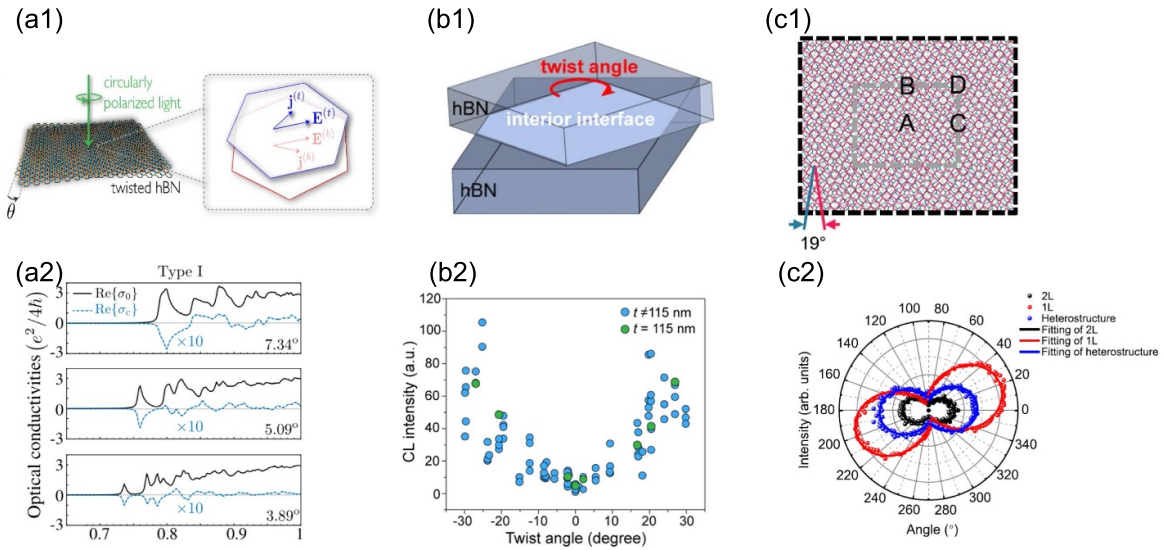


Figure 7. Optical properties of other twisted 2D materials. (a1) Illustration of twisted bilayer hBN with incident circularly light. Reprinted (figure) with permission from [196], Copyright (2020) by the American Physical Society. (a2) Real part of total (black lines) and chiral (blue lines) optical conductivity. Reprinted with permission from [196]. Copyright (2021) American Chemical Society. (b1) Twist-angle dependent cathodoluminescence (CL) intensity in (b1) twisted hBN multilayers. (b1) and (b2) Reprinted with permission from [197]. Copyright (2021) American Chemical Society. (c2) Anisotropic photoluminescence emissions in (c1) twisted monolayer/bilayer phosphorene heterostructure with twist angle 19° comparing to monolayer (1 L) and bilayer phosphorene (2 L). (c1) and (c2) Reproduced from [198]. CC BY 4.0.

On the theoretical side, we highlight the following works: in [186], the authors used a continuum model to study the frequency-dependent conductivity at different levels of chemical potential. Moon and Koshino [115] performed both tight-binding and continuum calculations of the optical conductivity, and analytically explained the optical selection rules in terms of the symmetry of the effective Hamiltonian. In addition, Stauber *et al* [121] calculated chemical potential dependent Drude weight of the optical conductivity in TBG by means of a continuum model. The excitonic effects, for instance, electron–hole interactions [187], and the self-consistent Hartree potential [188], were also investigated in the optical spectra of TBG. It was found that in TBG under strain [189], the peaks associated with transitions between the flat bands in the optical conductivity were highly sensitive to the direction of the strain. The effects of a magnetic field [190] and magnetic impurities on the optical conductivity [191], as well as optical activity in TBG have also been analyzed [192]. Analysis in stacking configurations [193, 194], quantum dots and large twist angles ($\theta \geq 5^\circ$) [195] reveals additional optical properties.

4.2. Optical properties of other twisted 2D materials

Owing to the chiral symmetry, twisted bilayer hBN displays circular dichroism, which has a different absorption of left and right circularly polarized light [199]. This property can be tuned by stacking and twisting [196]. The circular dichroism is proportional to the ratio of chiral conductivity to the total conductivity σ_0 (shown in figure 7(a2)). The chiral response indicated that twisted bilayer hBN had different absorption to left and right-polarized light. Besides twisted bilayer hBN, twisted

hBN films have also attracted recent experimental research, in particular Lee *et al* [197] found that both wavelength and intensity of luminescence were tunable. These properties were found to be enhanced with the twist angle between the hBN interface layers increased, as seen in figure 7(b2). The origin of this enhancement was that the moiré sub-band gap decreased with twist angle. This experiment indicates that the moiré potential is relevant in the moiré structures composed of bulk-like materials.

On the other hand, moiré optical properties in twisted semiconductors have also been investigated. For example, in the anisotropic twisted monolayer/bilayer phosphorene heterostructure, shown in figure 7(c1). The detected anisotropic optical transitions were notably different from the optical features of the corresponding monolayer and multilayer phosphorene [200, 201], even at a large angle like 19° , as illustrated in figure 7(c2). The reason behind this effect is that the moiré potential resulted in a strong hybridization between the twisted layers. Furthermore, the optical moiré transitions were sensitive to the twist angle [198]. Additionally, the twisted heterostructure of anisotropic materials such as black phosphorus and orthorhombic molybdenum trioxide can be used to control light polarization state [202]. Twisting large angles such as $\theta = 21.81^\circ$ and $\theta = 32.22^\circ$ can also serve as a way to reduce interlayer interaction of bilayer MoS_2 , which can induce a higher value of absorbance than untwisted case [203].

4.3. Plasmons of TBG

TBG offers new degrees of freedom on tuning the electromagnetic response, for example, the twist angle [187, 207, 208].

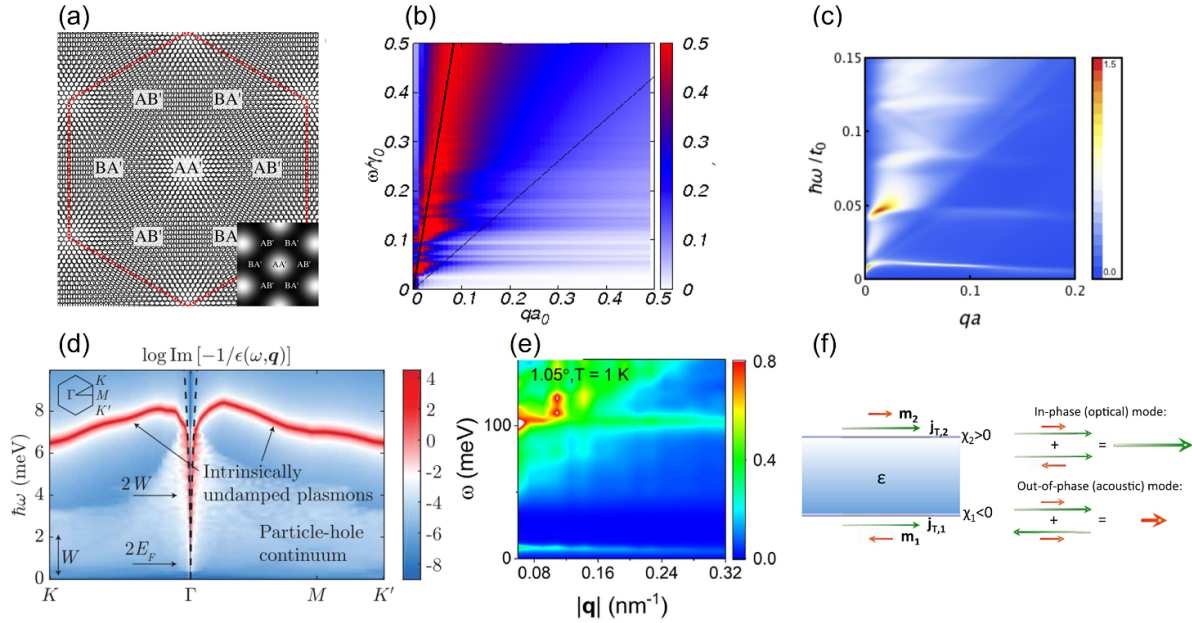


Figure 8. Theoretical exploration of plasmons in twisted bilayer graphene. (a) Moiré structure of twisted bilayer graphene. The moiré pattern contains AA, AB and BA high-symmetry stackings. Reproduced from [121]. CC BY 3.0. (b) Linear plasmon emerging in the loss function intensity plot of magic-angle twisted bilayer graphene. Reproduced from [121]. CC BY 3.0. (c) Density function plot of the loss function showing quasi-flat plasmons in twisted bilayer graphene at 1.61°. Reprinted with permission from [204]. Copyright (2016) American Chemical Society. (d) Undamped plasmons in doped magic-angle twisted bilayer graphene. W is the width of the narrow bands. E_F is the Fermi energy. Reproduced with permission from [205]. (e) Dispersion-less and low-damped plasmon appearing in the loss function spectrum of undoped magic-angle TBG at temperature $T = 1$ K. Reprinted (figure) with permission from [120], Copyright (2021) by the American Physical Society. (f) Chiral plasmon response in twisted bilayer graphene. Reprinted (figure) with permission from [206], Copyright (2017) by the American Physical Society.

Plasmons are collective charge oscillations that lead to nanoscale optical fields. One of the pioneer works was that of Stauber *et al* [121] who theoretically investigated the plasmonic spectrum of TBG via a continuum model. They found that the TBG interlayer coupling gave rise to a finite Drude weight, even in the undoped case. This allowed for the existence of plasmons that was weakly Landau-damped due to the quasi-localized nature of the interband transition states. As shown in figure 8(b), acoustic interband plasmon modes appeared at zero chemical potential and changed to conventional \sqrt{q} modes with non-zero doping levels in the first magic-angle (1.05°) TBG [121]. Moreover, plasmon modes in TBG were dependent on both twist angle and the chemical potential. Interestingly, quasi-flat plasmon modes and renormalized Fermi velocity (approached zero) were predicted in TBG even for twist angles ($\sim 1.61^\circ$) larger than the magic angle, as seen in figure 8(c). These collective excitations were explained as oscillation of localized states around the AA regions (see figure 8(a)) [204]. Moreover, intrinsically undamped and quasi-flat plasmon modes were discovered in doped magic-angle graphene, as depicted in figure 8(d) [205]. Conversely, at zero doping, including the effects of atomic relaxation, low-damped and damped plasmons were observed to emerge in the magic-angle configuration [120]. A further theoretical study found that in the long wavelength limit, the plasmon energy could be independent of doping level, but can be tuned by the bias voltage in magic-angle TBG [209]. These

findings distinguish the TBG system from the 2D electron gas (2DEG) that has a traditional \sqrt{q} plasmon dispersion with energy dependent on charge density [210]. Moreover, other unusual plasmon features such as plasmonic Dirac cone and plasmon non-reciprocity, were discovered in biased magic-angle TBG [211–214]. In addition, a further design of a TBG device as in figure 8(f), allowed to excite chiral longitudinal plasmonic modes with different phases. Additional chiral responses and plasmon edge states were exploited and were found to enhance the electromagnetic near-fields chirality in TBG [215–217]. Furthermore, theoretical studies explored how plasmon in TBG were influenced by electron–electron interaction [188, 218], finite size of TBG [219], and magnetic field [220].

Experimentally, the plasmon wavelength and damping rate were investigated by infrared s-SNOM with an excitation energy of 0.11 eV [221]. It was found that TBG with decreased twist angles led to the decrease of the plasmon wavelength, shown in figure 9(b), reflecting a renormalization of the Fermi velocity of the Dirac fermions at different twist angles. A reduced Fermi velocity is attributed to the enhanced interlayer interaction at twist angles, giving rise to a relaxation of the plasmon wavelength. However, the plasmon damping rate was found to be smaller with larger twist angles, as seen in figure 9(c), likely due to stronger charge scattering rates [221]. On the other hand, the propagation of plasmon polaritons was studied by infrared nano-imaging in TBG [101]. A

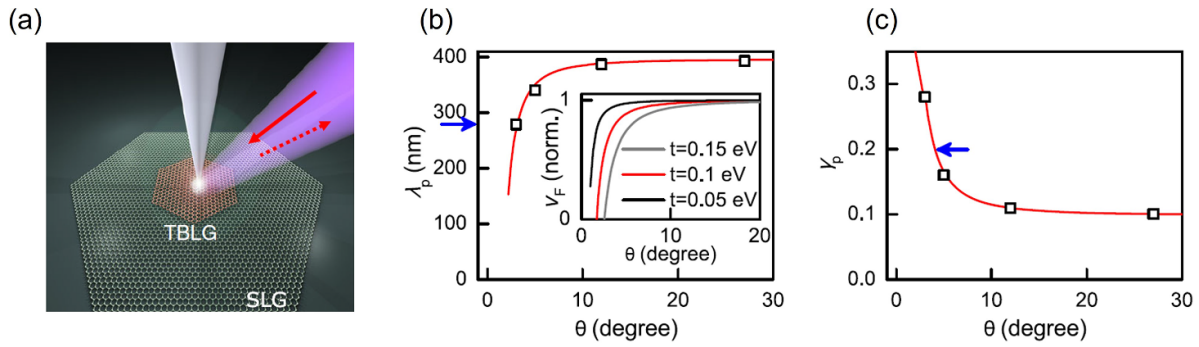


Figure 9. Experimental investigation of plasmons in twisted bilayer graphene. (a) Illustration of the nanoinfrared imaging experiment using s-SNOM in TBG using laser energy of $E = 0.11$ eV. (b) Plasmon wavelength of TBG versus twist angles. The insets plots the normalized Fermi velocity of TBG at different interlayer coupling energy t . (c) Plasmon damping rate at different twist angles. The blue arrows in (b) and (c) mark the value of plasmon wavelength and damping rate in single layer graphene, respectively. Reprinted (figure) with permission from [221], Copyright (2017) by the American Physical Society.

linear-like plasmon mode (that is, the dispersion of a plasmon mode is closely linear) of 1.35° TBG was observed by Hesp *et al* [98]. The plasmon mode had an energy around 220 meV, due to interband collective excitations whose spectrum was reproduced with a continuum model with reduced AA tunnel coupling.

In addition, chiral plasmons, the surface electromagnetic waves showing non-reciprocal propagation, in TBG were experimentally reported in [222]. They are achieved due to the uncompensated Berry flux of the electron gas under optical pumping. They were found to be characterized by two peaks appearing in the extinction spectra. These low-energy plasmon modes arose from interband transition with broken time-reversal and inversion symmetry. In the experiment, a plasmonic mode whose group velocity approaching to zero (termed slow plasmon modes) was identified around 0.4 eV, which stemmed from interband transition between subbands in lattice-relaxed AB domains [222], compared to theoretically predicted quasi-flat plasmon mode generated in the AA regions [204]. These slow plasmon modes could couple to light and form slow surface plasmon polaritons, which also provide potential for constructing optical metamaterials [223].

4.4. Plasmons of twisted multilayer graphene

Flat band and Dirac bands are found to coexist in twisted trilayer graphene with mirror symmetry [51, 54]. This coexistence may allow the plasmons to have different properties from those in TBG. Theoretically, Wu *et al* [224] numerically investigated plasmons in twisted trilayer graphene with different twist angles and vertical pressures. In particular, for a twist angle of 1.35° , the defined magic angle at which Fermi velocity is zero in this system, a clear quasi-flat plasmon mode emerged below 0.05 eV, as seen in figure 10(a). This plasmon was found to be originated from collective excitations inside the flat bands. As shown in figure 10(c), for large twist angles and no pressure, the quasi-flat plasmon mode had a blue shift to an energy of 0.06 eV indicating the presence of wider bands near charge neutrality. By applying a vertical pressure,

the plasmon mode reappeared, indicating an enhancement of the interlayer coupling with pressure.

On the other hand, numerical studies found that long lived, flat intraband and interband plasmons can exist in TDBG [225]. In particular, it was found that a flat intraband plasmon modes emerged at long momentum because of the influence of higher interband transitions. Furthermore, as shown in figures 10(d)–(f) these plasmon modes were found to be tuned by a vertical electric field, twist angle and doping, respectively. Gapped interband plasmon and intraband plasmon appeared at small and large electric field, respectively, and they persisted over a wide range of twist angles.

4.5. Plasmons of twisted bilayer TMDCs

In moiré TMDCs, the existence of flat bands also provides possibility to explore quasi-flat plasmon modes. A recent numerical study [226] suggested that both atomic relaxation and high energy bands have an impact on the low energy flat-band plasmon in twisted bilayer MoS₂, shown in figure 11. In particular, for an unrelaxed system, shown in figures 11(b1) and (c1), a flat intraband and linear interband plasmon modes were found. The distinct results between the different approximations suggested that the interband transitions play an important role in the unrelaxed system. However, the relaxation effects transformed the two plasmon modes to one mode with \sqrt{q} dispersion as seen in figures 11(b1) and (c2). Further analysis concluded that the isolation of the flat band shown in figure 11(d1) was the key to obtain quasi-flat plasmon modes in twisted bilayer TMDCs, and the high-energy interband transitions had impact on plasmons at a large momentum limit [226]. In addition to the twist angle effect on plasmons in twisted bilayer MoS₂, a recent experiment also showed that film thickness ratio of bilayers could manipulate plasmon topology in twisted WTe₂ films [227]. Single-layer MoS₂ could provide multi-component plasmons since it features spin and valley as two extra degree of freedom [228], which could be used to engineer the plasmon properties in twisted bilayer TMDCs in future studies.

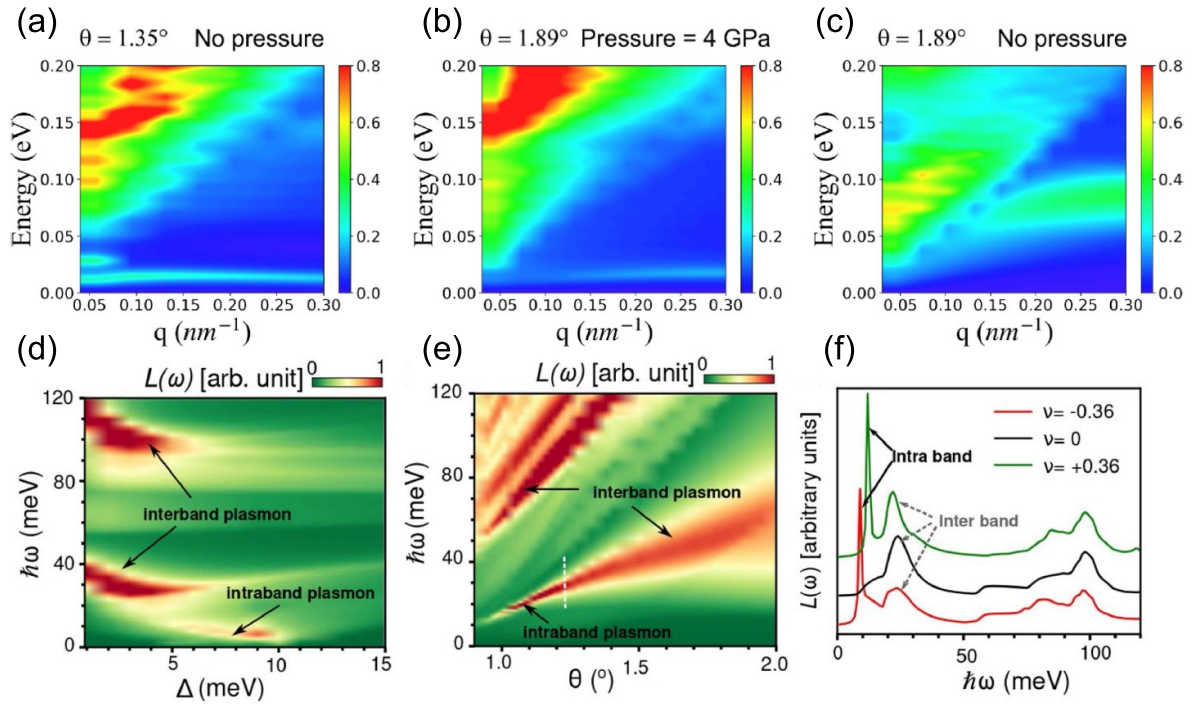


Figure 10. (a) Loss function intensity plots in the magic-angle 1.35° twisted trilayer graphene; Reprinted (figure) with permission from [224], Copyright (2021) by the American Physical Society. (b) and (c) pressure engineering plasmon modes in 1.89° twisted trilayer graphene. (b) and (c) Reprinted (figure) with permission from [224], Copyright (2021) by the American Physical Society. Twisted double bilayer graphene intraband and interband plasmons as a function of: (d) electric bias, (e) twist angle, and (f) doping level. (d)–(f) Reprinted (figure) with permission from [225], Copyright (2022) by the American Physical Society.

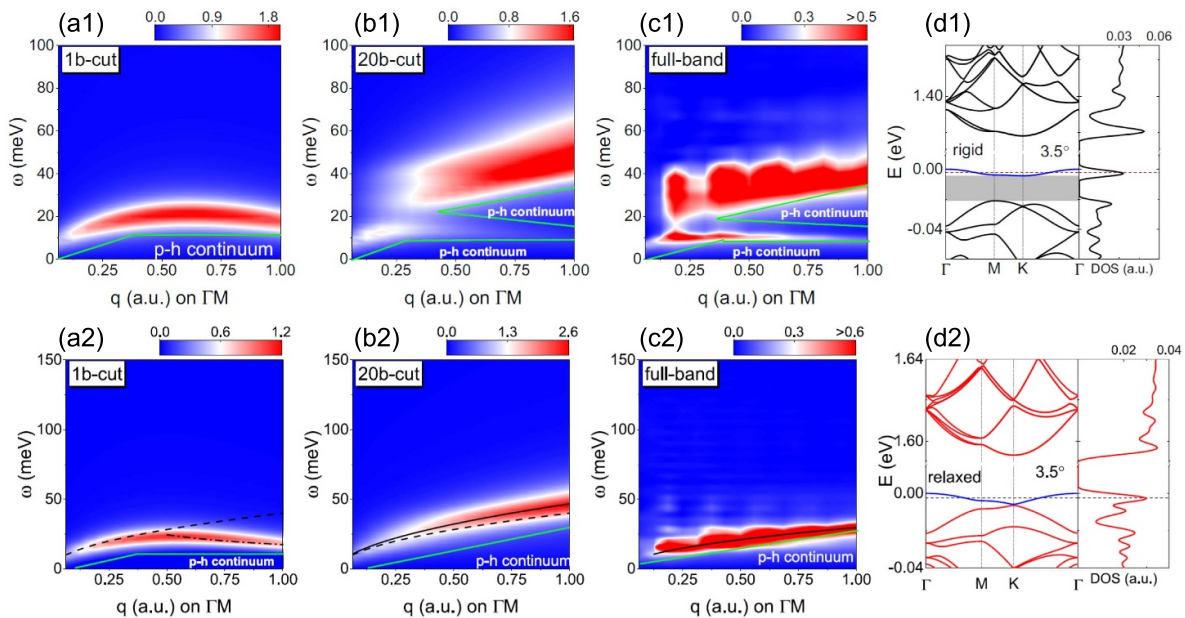


Figure 11. Loss function intensity plots of twisted bilayer MoS_2 with (first row) and without (second row) atomic relaxation. (a) Only one band, the flat band included in equation (6), while (b) 40 band near the flat band included and (c) full band of tight-binding model with TBPM as equation (7). Particle-hole (p)–(h) continuum region is marked with ‘p-h continuum’ and boundaries with green solid lines. (d) The band structure of 3.5° twisted bilayer MoS_2 without lattice relaxation (d1) and within (d2). Reprinted (figure) with permission from [226], Copyright (2022) by the American Physical Society.

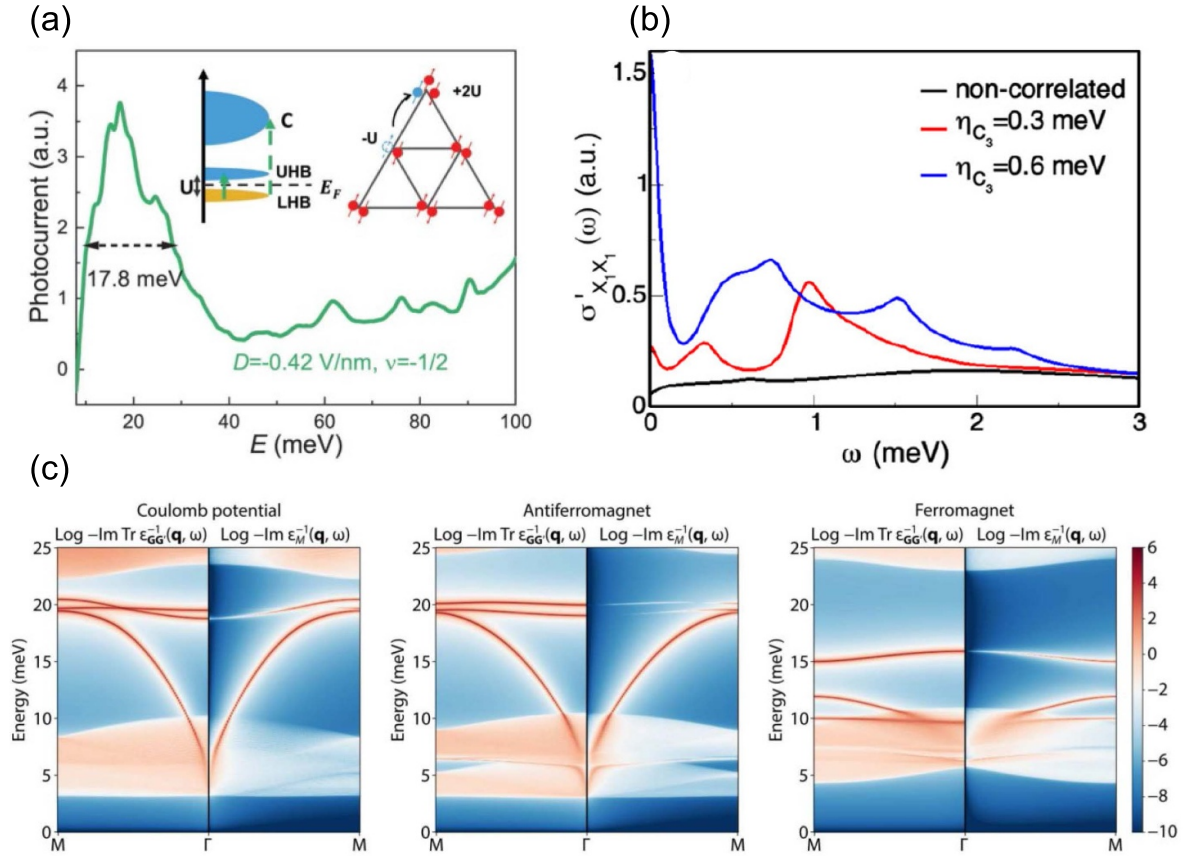


Figure 12. Many-body effects. (a) Observed optical response peak in correlated ABC trilayer graphene-hBN moiré structure. From [229]. Reprinted with permission from AAAS. The photocurrent peak corresponds to the optical transition crossing the Mott gap between lower Hubbard band (LHB) and upper Hubbard band (UHB), as illustrated by the solid arrow in the left inset. (b) Optical conductivity in TBG with correlated effect (nematic order, red and blue lines) and without correlated effect (black line). η_{C_3} is the magnitude of the nematic order. Reproduced from [185]. CC BY 4.0. (c) Plasmon spectrum of TBG within different many-body effect. Reproduced from [230]. CC BY 4.0.

5. Relation with other properties

5.1. Many-body effects

Many-body effects can provide a significant effect on optical properties and plasmons of moiré structures. For example, optical spectroscopy was employed to probe correlations in ABC rhombohedral trilayer graphene with hBN (ABC-hBN) [229]. In this work, an optical absorption peak emerged at ~ 18 meV, indicating a direct optical excitation across an emerging Mott insulator, as shown in figure 12(a). A similar optical spectra was observed at different fillings. The optical response was found to be a useful tool to characterize the onsite Coulomb repulsion energy, U , in the corresponding Hubbard model. On the other hand, optical conductivity was also theoretically used to reveal the nature of correlated states in TBG [185]. Comparing to the optical excitation that a Drude peak emerged at charge neutrality in non-correlated models, new absorption peaks appeared in the optical spectrum for different values of correlated nematic order parameters η_{C_3} , see figure 12(b). Additional calculations in the same system showed that the optical conductivity can be used to distinguish different symmetry broken states. The plasmons can also be used to probe many body effects as discussed

in section 4.1. Recently, Papaj and Lewandowski [230] proposed to probe correlated states with plasmons in twisted heterobilayer TMDCs, where a folded plasmon spectrum can be a signature of correlated states, as shown in figure 12(c). Here, the plasmon spectra has different characteristics depending on the type of correlated effects.

5.2. Non-linear optical response

The nonlinear optical response in TBG, also referred to as optotwistronics [232] or twistoptics [233], has attracted attention only recently. Theoretical works have explored the impact of light on the TBG band structure. In particular, a Floquet band engineering has been investigated by means of tight-binding models [234, 235]. Due to the extensive number of sites in the TBG moiré unit cell, the continuum model has proven to be highly valuable for studying optically induced flat bands [236], the manipulation of interlayer couplings [237], and the formulation of effective Floquet Hamiltonians [238].

As mentioned in the previous section, the TBG transition energies are notably influenced by the twist angle [239, 240]. Consequently, for a constant twist angle, the activation or deactivation of one- and two-photon resonances

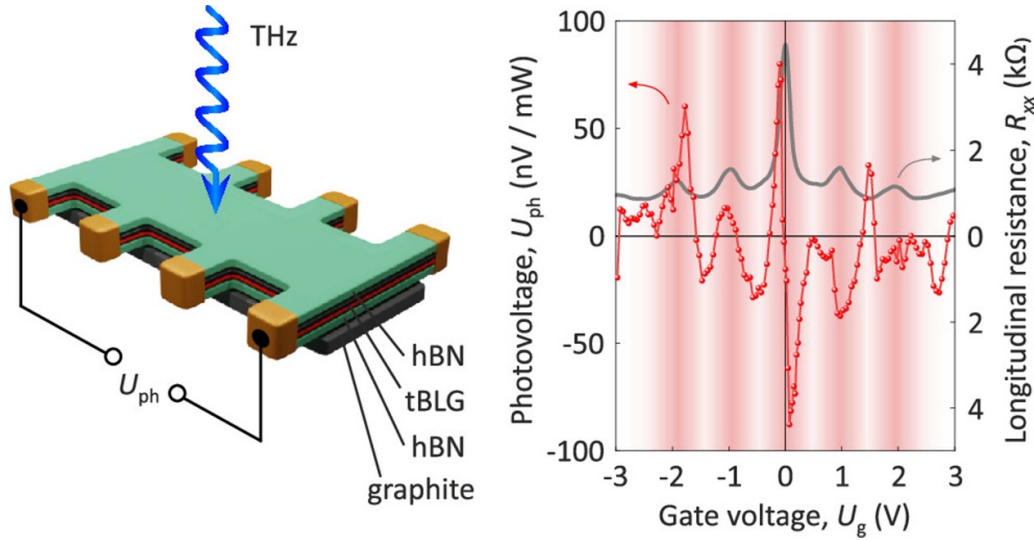


Figure 13. Photogalvanic effect in low angle TBG ($\theta = 0.6^\circ$). (Left side) Schematics of a TBG sample encapsulated by hBN. (Right side) An incident terahertz radiation gives rise to a photovoltage. Reprinted with permission from [231]. Copyright (2020) American Chemical Society.

can be achieved by adjusting the incident wavelength. This characteristic allows for a highly adaptable second harmonic generation in TBG [241, 242]. Remarkably, at larger twist angles ($\sim 21.79^\circ$) and in the presence of intense laser fields, TBG has been found to display high-harmonic generation, that by symmetry grounds cannot occur in monolayer or bilayer graphene [232, 243]. The selection rules described in [232] under circularly polarized light stem from the underlying lattice symmetry of TBG at large angles.

On the other hand, at low twist angles ($\sim 1.05^\circ$) there is an interplay between twist, band geometry and optical response [243]. There is an emergence of dynamical symmetries coupled with the standard symmetries of the TBG lattice (C_{2y} and C_3) which are not present at large twist angles ($\sim 21.79^\circ$). Additional selection rules for the current response are obtained at the low angle regime. In particular, an induced inversion symmetry breaking [244] in the bilayer system allows for a non-zero finite Berry curvature which enhances the non-linearity. Interestingly, as described in [243] the high order harmonics were found strongly dependent on the magnitude of the band geometry through the Berry curvature. The photogalvanic effect, which is the lowest order non-linear effect, was predicted [231, 245] and then experimentally observed in low-angle ($\sim 0.6^\circ$) samples of TBG [231], see figure 13. At higher orders, a third order optical non-linearity was also reported [246], where the non-linear response was found to be considerably modified depending on the rotation angle in TBG. Effects of the band topology [247], high harmonic generation [248], correlated insulating states [249] have also been investigated. In addition to TBG, non-linear optical response can be achieved in large-angle ($\sim 50^\circ$) twisted multilayer WS_2 [250]. It is worthy to mention that via a second harmonic generation in heterostructures of graphene-hBN a transition from a commensurate to a non-commensurate state was detected [251].

5.3. Superconductivity

The origin of superconductivity in moiré twisted graphene layers remains a subject of debate [12, 257]. In addition to the proposed phonon-mediated theory [258, 259], purely electronic mechanisms such as the Kohn–Luttinger (KL) mechanism and plasmon-mediated superconductivity have also been examined [253, 255, 256]. This is motivated by the significant influence of electron–electron interactions found in magic-angle TBG [15, 18]. For instance, theoretical studies of the dielectric function within the RPA, cf equation (10), reveal that the screened Coulomb potential calculated near the magic-angle TBG displays attractive regions in real space [253, 254, 260], see figure 14(a), indicating that superconductivity could be induced by pure electron–electron interactions [261, 262] through a KL mechanism [253, 263]. The RPA calculations with frequency-independent polarization function show that the superconducting instability can appear near VHS and precedes a spin-density-wave instability under KL mechanism, as shown in figure 14(b). Furthermore, the critical temperature has also been predicted based on the KL mechanism by calculating the static screened dielectric function and the gap equation [262]. However, it is worth noting that the predicted critical temperature is not as high as what has been observed in experiments, as indicated by the gray dots in figure 14(c). This suggests that phonons may also contribute to the enhancement of the superconducting pairing [254].

On the other hand, as depicted in figure 14(d), the intrinsic plasmon mode in magic-angle TBG is estimated to lead to an even higher critical temperature (T_c) than the effects of phonons under a massless Dirac model. Further numerical calculations reveal that the dynamical Coulomb-driven T_c can reach approximately 15 K and varies with the electron density of TBG near the magic angle, as shown in figure 14(e). Further research delves into how the LFE plays a role in cooperative

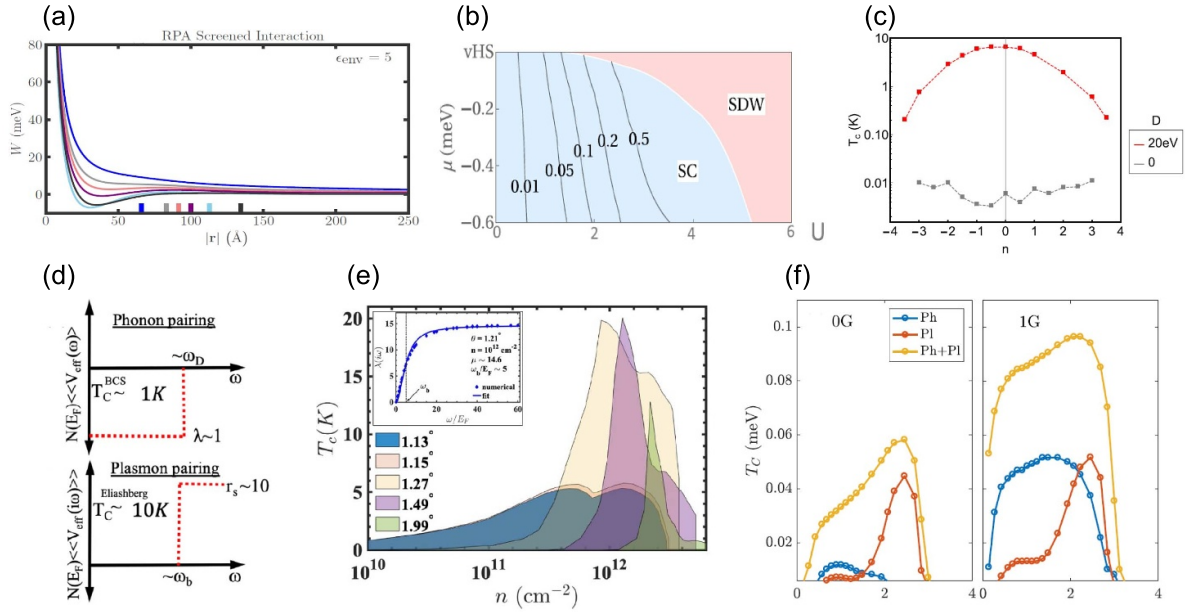


Figure 14. (a) Attractive electron–electron interaction in magic-angle twisted bilayer graphene. Reprinted (figure) with permission from [252], Copyright (2019) by the American Physical Society. (b) Purely electron–electron induced superconductor phase in magic-angle twisted bilayer graphene. Reprinted (figure) with permission from [253], Copyright (2019) by the American Physical Society. (c) Superconductivity critical temperature explained by electron–electron screening potential with (red dots) and without phonon effect (gray dots). Reproduced with permission from [254]. (d) Plasmon pairing driven by dynamic Coulomb interaction comparing to Phonon pairing and (e) critical temperature of plasmon-mediated superconductivity in TBG at different angles. (d) and (e) Reproduced from [255]. CC BY 4.0. (f) Phonon (Ph) and plasmon (Pl) mediated superconductivity in magic-angle TBG without (0G) and within (1G) local field effect. Reprinted (figure) with permission from [256], Copyright (2021) by the American Physical Society.

effects between plasmons and phonons on superconductivity [256]. As illustrated in figure 14(f), plasmon-mediated superconductivity appears to be insensitive to LFE, which aligns with previous findings indicating that plasmons in TBG are not significantly affected by LFE [204, 205]. Recently, extrinsic screening effects on superconductivity were investigated in TBG as well, showing that the critical temperature was unaffected by screening unless the screening layer was lower than three nanometers from the superconductor [264]. Besides LFE, effect of vertex corrections on plasmon-mediated superconductivity in moiré structures could deserve some attentions [265], while vertex corrections could be safely dropped in conventional high-density superconductors according to Migdal’s theorem [266, 267].

6. Summary and outlook

This paper reviews recent theoretical and experimental research on optical properties and plasmons in widespread non-twisted and twisted moiré structures. For non-twisted moiré graphene-based structures, the moiré potential plays a key role in producing saddle points in the miniband structure of graphene, which gives rise to new optical interband transitions between VHS which are ultimately reflected in the experimental optical conductivity and interband plasmons. In particular, particle-hole asymmetric features in optical conductivity and plasmons emerged due to moiré potential breaking the symmetry of electronic wavefunction in graphene-hBN

structure. The moiré-induced interband plasmons and intrinsic intraband plasmon can coexist in graphene-based non-twisted moiré heterostructures. In twisted moiré structures, changing the twist angle results in varying moiré lengths, leading to a reshaping of the band structure and alterations in both bandwidth and band velocity. In most studies on TBG, the optical absorption peaks and plasmon wavelengths exhibit a red shift as the twist angle decreases. Additionally, interband plasmons, low-damped, and slow plasmon modes have been theoretically explored in flat-band TBG and confirmed by experiments. These findings have spurred further investigations into plasmonics in flat-band twisted trilayer graphene, double bilayer graphene, and twisted TMD systems. Twisting is also recognized as a means to modulate the optical response in other twisted 2D moiré systems that also exhibit intriguing optical phenomena. In flat-band moiré structures, electron–electron interactions can also have an impact on the optical response. Some studies have focused on understanding the effects of these interactions through optical dynamics and plasmonics. Additionally, the formation of superconducting electron pairs through plasmon and electron–electron interactions under the random phase approximation provides insights into the mechanisms underlying superconductivity in moiré structures.

Prosperous and tremendous theoretical and experimental studies on moiré structures are still ongoing to open new avenues for physics and potential applications. Twist-angle induced moiré potentials are appearing in other structures, such as moiré of moiré graphene layers [268–270], TBG-hBN heterostructure [271–274], TBG-TMDC heterostructure

[27], twisted three-dimensional systems [275–277], and so on. Beyond aforementioned non-twisted moiré heterostructures, studies of MoS₂-metal moiré systems [278], and non-twisted TMDC bilayer moiré heterostructures such as MoTe₂/WSe₂ are also arising [279, 280]. These moiré structures could also be ideal platforms for exploring interesting linear and non-linear optical properties as well as plasmonics. For example, spin–orbit coupling accompanying with the moiré potentials could cause more optical transitions in TBG-TMDC systems; the hBN induced band gap could change the plasmon energy in TBG-hBN moiré structures. In addition, the twist-angle and electron–electron interaction effect can also be important in aligned graphene-based heterostructures in prospective studies. Disorder effects, such as twist-angle and strain effects, have shown an impact on electronic and transport properties in moiré structures [281–285]. More studies of disorder effects on optical properties of moiré structures are also needed in future. Last but not least, although the optical and plasmonic applications of moiré structures are not the primary focus of this topic review they deserve further investigation and attention.

Finally, by creating moiré patterns and further tuning them as needed (e.g. by adjusting the twist angle, combining different materials, and applying artificial structure potentials [286]), we can obtain control over the manipulation of light in future state-of-the-art technologies. This control may find applications in moiré photonics and moiré optoelectronics, including lasers, detectors, modulators, infrared/terahertz photoresponses, and polarizers. Exploring and gaining a fundamental understanding of how the moiré potential influences the optoelectronic properties of these materials is, therefore, crucial for the advancement of the field.

Data availability statement


No new data were created or analyzed in this study.

Acknowledgments

We thank Tommaso Cea, Alejandro Jimeno-Pozo, Héctor Sainz-Cruz, Yunhai Li, Zewen Wu, Yonggang Li for fruitful discussions. IMDEA Nanociencia acknowledges support from the ‘Severo Ochoa’ Programme for Centres of Excellence in R&D (CEX2020-001039-S/AEI/10.13039/501100011033). P A P, J A S-G, F G and Z Z acknowledge support from NOVOMAT, Grant PID2022-142162NB-I00 funded by MCIN/AEI/ 10.13039/501100011033 and, by ‘ERDF A way of making Europe. P A P and F G acknowledge funding from the European Commission, within the Graphene Flagship, Core 3, Grant Number 881603 and from grants NMAT2D (Comunidad de Madrid, Spain), SprQuMat and (MAD2D-CM)-MRR MATERIALES AVANZADOS-IMDEA-NC. S Y acknowledges support funding from the National Natural Science Foundation of China (No. 12174291) and Natural Science Foundation of Hubei Province, China (Grant No. 2022BAA017). Z Z acknowledges support funding from the

European Union’s Horizon 2020 research and innovation programme under the Marie Skłodowska-Curie Grant Agreement No. 101034431.

ORCID iDs

Xueheng Kuang  <https://orcid.org/0009-0007-7233-9512>
 Pierre A Pantaleón Peralta  <https://orcid.org/0000-0003-1709-7868>
 Jose Angel Silva-Guillén  <https://orcid.org/0000-0002-0483-5334>
 Shengjun Yuan  <https://orcid.org/0000-0001-6208-1502>
 Francisco Guinea  <https://orcid.org/0000-0001-5915-5427>
 Zhen Zhan  <https://orcid.org/0000-0002-1575-7722>

References

- [1] Novoselov K S, Geim A K, Morozov S V, Jiang D E, Zhang Y, Dubonos S V, Grigorieva I V and Firsov A A 2004 *Science* **306** 666–9
- [2] Lin Y, Williams T V and Connell J W 2010 *J. Phys. Chem. Lett.* **1** 277–83
- [3] Weng Q, Wang X, Wang X, Bando Y and Golberg D 2016 *Chem. Soc. Rev.* **45** 3989–4012
- [4] Chhowalla M, Shin H S, Eda G, Li L-J, Loh K P and Zhang H 2013 *Nat. Chem.* **5** 263–75
- [5] Manzeli S, Ovchinnikov D, Pasquier D, Yazyev O V and Kis A 2017 *Nat. Rev. Mater.* **2** 17033
- [6] Li L, Yu Y, Ye G J, Ge Q, Ou X, Wu H, Feng D, Chen X H and Zhang Y 2014 *Nat. Nanotechnol.* **9** 372–7
- [7] Ji J *et al* 2016 *Nat. Commun.* **7** 13352
- [8] Roldán R, Chirrolli L, Prada E, Silva-Guillén J A, San-Jose P and Guinea F 2017 *Chem. Soc. Rev.* **46** 4387–99
- [9] Geim A K and Grigorieva I V 2013 *Nature* **499** 419–25
- [10] Dean C, Young A, Wang L, Meric I, Lee G H, Watanabe K, Taniguchi T, Shepard K, Kim P and Hone J 2012 *Solid State Commun.* **152** 1275–82
- [11] Andrei E Y and MacDonald A H 2020 *Nat. Mater.* **19** 1265–75
- [12] Andrei E Y, Efetov D K, Jarillo-Herrero P, MacDonald A H, Mak K F, Senthil T, Tutuc E, Yazdani A and Young A F 2021 *Nat. Rev. Mater.* **6** 201–6
- [13] Suárez Morell E, Correa J D, Vargas P, Pacheco M and Barticevic Z 2010 *Phys. Rev. B* **82** 125413
- [14] Bistrizter R and MacDonald A H 2011 *Proc. Natl Acad. Sci.* **108** 12233–7
- [15] Cao Y, Fatemi V, Fang S, Watanabe K, Taniguchi T, Kaxiras E and Jarillo-Herrero P 2018 *Nature* **556** 43–50
- [16] Yankowitz M, Chen S, Polshyn H, Zhang Y, Watanabe K, Taniguchi T, Graf D, Young A F and Dean C R 2019 *Science* **363** 1059–64
- [17] Oh M, Nuckolls K P, Wong D, Lee R L, Liu X, Watanabe K, Taniguchi T and Yazdani A 2021 *Nature* **600** 240–5
- [18] Cao Y *et al* 2018 *Nature* **556** 80–84
- [19] Choi Y, Kemmer J, Peng Y, Thomson A, Arora H, Polski R, Zhang Y, Ren H, Alicea J and Refael G E A 2019 *Nat. Phys.* **15** 1174–80
- [20] Xie Y, Lian B, Jäck B, Liu X, Chiu C L, Watanabe K, Taniguchi T, Bernevig B A and Yazdani A 2019 *Nature* **572** 101–5
- [21] Kerelsky A *et al* 2019 *Nature* **572** 95–100
- [22] Liu X, Wang Z, Watanabe K, Taniguchi T, Vafeek O and Li J I 2021 *Science* **371** 1261–5
- [23] Xie Y *et al* 2021 *Nature* **600** 439–43
- [24] Choi Y *et al* 2021 *Nature* **589** 536–41

- [25] Pons R, Mielke A and Stauber T 2020 *Phys. Rev. B* **102** 235101
- [26] Bhowmik S *et al* 2023 *Nat. Commun.* **14** 4055
- [27] Lin J X, Zhang Y H, Morissette E, Wang Z, Liu S, Rhodes D, Watanabe K, Taniguchi T, Hone J and Li J I A 2022 *Science* **375** 437–41
- [28] Li Z and Wang Z 2020 *Chin. Phys. B* **29** 107101
- [29] Tseng C C, Ma X, Liu Z, Watanabe K, Taniguchi T, Chu J H and Yankowitz M 2022 *Nat. Phys.* **18** 1038–42
- [30] Duan J, Jian Y, Gao Y, Peng H, Zhong J, Feng Q, Mao J and Yao Y 2022 *Phys. Rev. Lett.* **129** 186801
- [31] Zhu Z, Carr S, Massatt D, Luskin M and Kaxiras E 2020 *Phys. Rev. Lett.* **125** 116404
- [32] Park Y, Chittari B L and Jung J 2020 *Phys. Rev. B* **102** 1–14
- [33] Wu Z, Zhan Z and Yuan S 2021 *Sci. China Phys. Mech. Astron.* **64** 267811
- [34] Chebrolu N R, Chittari B L and Jung J 2019 *Phys. Rev. B* **99** 235417
- [35] Rickhaus P *et al* 2019 *Nano Lett.* **19** 8821–8
- [36] Haddadi F, Wu Q S, Kruchkov A J and Zazyev O V 2020 *Nano Lett.* **20** 2410–5
- [37] Rickhaus P *et al* 2021 *Science* **373** 1257–60
- [38] Naik M H and Jain M 2018 *Phys. Rev. Lett.* **121** 266401
- [39] Venkateswarlu S, Honecker A and Trambly De Laissardière G 2020 *Phys. Rev. B* **102** 81103
- [40] Zhan Z, Zhang Y, Lv P, Zhong H, Yu G, Guinea F, Silva-Guillén J A and Yuan S 2020 *Phys. Rev. B* **102** 241106
- [41] Vitale V, Atalar K, Mostofi A A and Lischner J 2021 *2D Mater.* **8** 045010
- [42] Shabani S, Halbertal D, Wu W, Chen M, Liu S, Hone J, Yao W, Basov D N, Zhu X and Pasupathy A N 2021 *Nat. Phys.* **17** 720–5
- [43] Devakul T, Crépel V, Zhang Y and Fu L 2021 *Nat. Commun.* **12** 6730
- [44] Zhang Y, Liu T and Fu L 2021 *Phys. Rev. B* **103** 155142
- [45] Xian L, Kennes D M, Tancogne-Dejean N, Altarelli M and Rubio A 2019 *Nano Lett.* **19** 4934–40
- [46] Zhao X J, Yang Y, Zhang D B and Wei S H 2020 *Phys. Rev. Lett.* **124** 086401
- [47] Walet N R and Guinea F 2021 *Phys. Rev. B* **103** 125427
- [48] Woods C R, Ares P, Nevison-Andrews H, Holwill M J, Fabregas R, Guinea F, Geim A K, Novoselov K S, Walet N R and Fumagalli L 2021 *Nat. Commun.* **12** 347
- [49] Cao Y, Rodan-Legrain D, Rubies-Bigorda O, Park J M, Watanabe K, Taniguchi T and Jarillo-Herrero P 2020 *Nature* **583** 215–20
- [50] Shen C *et al* 2020 *Nat. Phys.* **16** 520–5
- [51] Park J M, Cao Y, Watanabe K, Taniguchi T and Jarillo-Herrero P 2021 *Nature* **590** 249–55
- [52] He M, Li Y, Cai J, Liu Y, Watanabe K, Taniguchi T, Xu X and Yankowitz M 2021 *Nat. Phys.* **17** 26–30
- [53] Kim H, Choi Y, Lewandowski C, Thomson A, Zhang Y, Polski R, Watanabe K, Taniguchi T, Alicea J and Nadj-Perge S 2022 *Nature* **606** 494–500
- [54] Hao Z, Zimmerman A, Ledwith P, Khalaf E, Najafabadi D H, Watanabe K, Taniguchi T, Vishwanath A and Kim P 2021 *Science* **371** 1133–8
- [55] Chen S *et al* 2021 *Nat. Phys.* **17** 374–80
- [56] Park J M, Cao Y, Xia L Q, Sun S, Watanabe K, Taniguchi T and Jarillo-Herrero P 2022 *Nat. Mater.* **21** 877–83
- [57] Zhang Y *et al* 2022 *Science* **377** 1538–43
- [58] Burg G W, Khalaf E, Wang Y, Watanabe K, Taniguchi T and Tutuc E 2022 *Nat. Mater.* **21** 884–9
- [59] Zhu G Y, Xiang T and Zhang G M 2018 *Sci. Bull.* **63** 1087–91
- [60] Chen G *et al* 2019 *Nat. Phys.* **15** 237–41
- [61] Chittari B L, Chen G, Zhang Y, Wang F and Jung J 2019 *Phys. Rev. Lett.* **122** 16401
- [62] Chen G *et al* 2020 *Nature* **579** 56–61
- [63] Sun X *et al* 2021 *Nat. Commun.* **12** 7196
- [64] Wang L *et al* 2020 *Nat. Mater.* **19** 861–6
- [65] Zhang Z, Wang Y, Watanabe K, Taniguchi T, Ueno K, Tutuc E and LeRoy B J 2020 *Nat. Phys.* **16** 1093–6
- [66] Zang J, Wang J, Cano J and Millis A J 2021 *Phys. Rev. B* **104** 075150
- [67] Xu Y, Kang K, Watanabe K, Taniguchi T and Mak K F 2022 *Nat. Nanotechnol.* **17** 934–9
- [68] Cai J *et al* 2023 *Nature* **622** 1–3
- [69] Zeng Y, Xia Z, Kang K, Zhu J, Knüppel P, Vaswani C, Watanabe K, Taniguchi T, Mak K F and Shan J 2023 *Nature* **622** 69–73
- [70] Park H *et al* 2023 *Nature* **622** 1–3
- [71] Xu F *et al* 2023 *Phys. Rev. X* **13** 031037
- [72] Andersen T I *et al* 2021 *Nat. Mater.* **20** 480–7
- [73] Du L, Molas M R, Huang Z, Zhang G, Wang F and Sun Z 2023 *Science* **379** eadg0014
- [74] Mak K F, Sfeir M Y, Wu Y, Lui C H, Misewich J A and Heinz T F 2008 *Phys. Rev. Lett.* **101** 196405
- [75] Mak K F, Ju L, Wang F and Heinz T F 2012 *Solid State Commun.* **152** 1341–9
- [76] Rukelj Z, Štrkalj A and Despoja V 2016 *Phys. Rev. B* **94** 1–11
- [77] Johari P and Shenoy V B 2011 *ACS Nano* **5** 5903–8
- [78] Li Y, Chernikov A, Zhang X, Rigosi A, Hill H M, Van Der Zande A M, Chenet D A, Shih E M, Hone J and Heinz T F 2014 *Phys. Rev. B* **90** 205422
- [79] Laturia A, Van de Put M L and Vandenberghe W G 2018 *npj 2D Mater. Appl.* **2** 6
- [80] Scholz A, Stauber T and Schliemann J 2013 *Phys. Rev. B* **88** 035135
- [81] Cox J D, Silveiro I and García de Abajo F J 2016 *ACS Nano* **10** 1995–2003
- [82] Koppens F H, Chang D E and García de Abajo F J 2011 *Nano Lett.* **11** 3370–7
- [83] Xiao S, Zhu X, Li B H and Mortensen N A 2016 *Front. Phys.* **11** 1–13
- [84] Gonçalves P A D and Peres N M 2016 *An Introduction to Graphene Plasmonics* (World Scientific)
- [85] Reserbat-Plantey A, Epstein I, Torre I, Costa A T, Gonçalves P, Mortensen N A, Polini M, Song J C, Peres N M and Koppens F H 2021 *ACS Photonics* **8** 85–101
- [86] Low T and Avouris P 2014 *ACS Nano* **8** 1086–101
- [87] Vakil A and Engheta N 2011 *Science* **332** 1291–4
- [88] Stauber T 2014 *J. Phys.: Condens. Matter* **26** 123201
- [89] Wang Y *et al* 2015 *Nano Lett.* **15** 883–90
- [90] Groenewald R, Rösner M, Schönhoff G, Haas S and Wehling T 2016 *Phys. Rev. B* **93** 205145
- [91] Li Y, Li Z, Chi C, Shan H, Zheng L and Fang Z 2017 *Adv. Sci.* **4** 1600430
- [92] Torbatian Z and Asgari R 2017 *J. Phys.: Condens. Matter* **29** 465701
- [93] Sunku S S *et al* 2020 *Nano Lett.* **20** 2958–64
- [94] Catarina G, Amorim B, Castro E V, Lopes J and Peres N 2019 *Handbook of Graphene* **3** 177–232
- [95] Deng B, Ma C, Wang Q, Yuan S, Watanabe K, Taniguchi T, Zhang F and Xia F 2020 *Nat. Photon.* **14** 549–53
- [96] Aizpurua J, Taubner T, de Abajo F J G, Brehm M and Hillenbrand R 2008 *Opt. Express* **16** 1529–45
- [97] Ni G X *et al* 2015 *Nat. Mater.* **14** 1217–22
- [98] Hesp N C *et al* 2021 *Nat. Phys.* **17** 1162–8
- [99] Polman A, Kociak M and de Abajo F J G 2019 *Nat. Mater.* **18** 1158–71
- [100] Yan X *et al* 2021 *Nature* **589** 65–69
- [101] Sunku S S *et al* 2018 *Science* **1156** 1153–6
- [102] Kubo R 1957 *J. Phys. Soc. Japan* **12** 570–86
- [103] Calderin L, Karasiev V V and Trickey S B 2017 *Comput. Phys. Commun.* **221** 118–42

- [104] Yuan S, De Raedt H and Katsnelson M I 2010 *Phys. Rev. B* **82** 115448
- [105] Li Y, Zhan Z, Kuang X, Li Y and Yuan S 2023 *Comput. Phys. Commun.* **285** 108632
- [106] Yu G, Wu Z, Zhan Z, Katsnelson M I and Yuan S 2019 *npj Comput. Mater.* **5** 122
- [107] Ahn S J *et al* 2018 *Science* **361** 782–6
- [108] Yao W *et al* 2018 *Proc. Natl Acad. Sci.* **115** 6928–33
- [109] Pezzini S *et al* 2020 *Nano Lett.* **20** 3313–9
- [110] Moon P, Koshino M and Son Y W 2019 *Phys. Rev. B* **99** 165430
- [111] Yuan S, Roldán R, De Raedt H and Katsnelson M I 2011 *Phys. Rev. B* **84** 195418
- [112] Roche S 1999 *Phys. Rev. B* **59** 2284
- [113] Fan Z, Garcia J H, Cummings A W, Barrios-Vargas J E, Panhans M, Harju A, Ortmann F and Roche S 2021 *Phys. Rep.* **903** 1–69
- [114] Kuzmenko A 2005 *Rev. Sci. Instrum.* **76** 083108
- [115] Moon P and Koshino M 2013 *Phys. Rev. B* **87** 205404
- [116] Mahan G D 2000 *Many-Particle Physics* (Springer)
- [117] Giuliani G and Vignale G 2008 *Quantum Theory of the Electron Liquid* (Cambridge University Press)
- [118] Coleman P 2015 *Introduction to Many-Body Physics* (Cambridge University Press)
- [119] Yuan S, Roldán R and Katsnelson M I 2011 *Phys. Rev. B* **84** 35439
- [120] Kuang X, Zhan Z and Yuan S 2021 *Phys. Rev. B* **103** 115431
- [121] Stauber T, San-Jose P and Brey L 2013 *New J. Phys.* **15** 113050
- [122] Maier S A *et al* 2007 *Plasmonics: Fundamentals and Applications* vol 1 (Springer)
- [123] Morawetz K, Ashokan V, Bala R and Pathak K N 2018 *Phys. Rev. B* **97** 155147
- [124] Kotov V N, Uchoa B and Neto A C 2008 *Phys. Rev. B* **78** 035119
- [125] Sabio J, Nilsson J and Neto A C 2008 *Phys. Rev. B* **78** 075410
- [126] Abedinpour S H, Vignale G, Principi A, Polini M, Tse W K and MacDonald A 2011 *Phys. Rev. B* **84** 045429
- [127] Gangadharaiah S, Farid A and Mishchenko E 2008 *Phys. Rev. Lett.* **100** 166802
- [128] Inaoka T, Nagao T, Hasegawa S, Hildebrandt T and Henzler M 2002 *Phys. Rev. B* **66** 245320
- [129] Singwi K, Tosi M, Land R and Sjölander A 1968 *Phys. Rev.* **176** 589
- [130] Jonson M 1976 *J. Phys. C: Solid State Phys.* **9** 3055
- [131] Neilson D, Świerkowski L, Sjölander A and Szymański J 1991 *Phys. Rev. B* **44** 6291
- [132] March N and Tosi M 1995 *Adv. Phys.* **44** 299–386
- [133] Adler S L 1962 *Phys. Rev.* **126** 413
- [134] Wisner N 1963 *Phys. Rev.* **129** 62
- [135] Louie S G, Chelikowsky J R and Cohen M L 1975 *Phys. Rev. Lett.* **34** 155
- [136] Van Vechten J and Martin R M 1972 *Phys. Rev. Lett.* **28** 446
- [137] Sturm K 1978 *Phys. Rev. Lett.* **40** 1599
- [138] Yang L, Deslippe J, Park C H, Cohen M L and Louie S G 2009 *Phys. Rev. Lett.* **103** 186802
- [139] Xue J, Sanchez-Yamagishi J, Bulmash D, Jacquod P, Deshpande A, Watanabe K, Taniguchi T, Jarillo-Herrero P and LeRoy B J 2011 *Nat. Mater.* **10** 282–5
- [140] Wang L, Zihlmann S, Liu M H, Makk P, Watanabe K, Taniguchi T, Baumgartner A and Schonenberger C 2019 *Nano Lett.* **19** 2371–6
- [141] Wang E *et al* 2016 *Nat. Phys.* **12** 1111–5
- [142] Shi Z *et al* 2014 *Nat. Phys.* **10** 743–7
- [143] Wallbank J R, Patel A A, Mucha-Kruczyński M, Geim A K and Fal'ko V I 2013 *Phys. Rev. B* **87** 245408
- [144] Nakagahara K and Wakabayashi K 2022 *Phys. Rev. B* **106** 075403
- [145] DaSilva A M, Jung J, Adam S and MacDonald A H 2015 *Phys. Rev. B* **92** 155406
- [146] Abergel D S and Mucha-Kruczyński M 2015 *Phys. Rev. B* **92** 115430
- [147] Liu B *et al* 2023 *Phys. Rev. Lett.* **131** 016201
- [148] Hwang E and Sarma S D 2007 *Phys. Rev. B* **75** 205418
- [149] Eberlein T, Bangert U, Nair R R, Jones R, Gass M, Bleloch A L, Novoselov K S, Geim A and Briddon P R 2008 *Phys. Rev. B* **77** 233406
- [150] Tomadin A, Guinea F and Polini M 2014 *Phys. Rev. B* **90** 161406
- [151] Tomadin A, Polini M and Jung J 2019 *Phys. Rev. B* **99** 035432
- [152] Bandurin D A *et al* 2018 *Nat. Commun.* **9** 5392
- [153] Yankowitz M, Xue J, Cormode D, Sanchez-Yamagishi J D, Watanabe K, Taniguchi T, Jarillo-Herrero P, Jacquod P and LeRoy B J 2012 *Nat. Phys.* **8** 382–6
- [154] Politano A, Slotman G J, Roldán R, Chiarello G, Campi D, Katsnelson M I and Yuan S 2017 *2D Mater.* **4** 021001
- [155] Despoja V, Novko D, Lončarić I, Golenić N, Marušić L and Silkin V M 2019 *Phys. Rev. B* **100** 195401
- [156] Politano A, Marino A, Formoso V, Farías D, Miranda R and Chiarello G 2011 *Phys. Rev. B* **84** 033401
- [157] Politano A, Marino A and Chiarello G 2012 *Phys. Rev. B* **86** 085420
- [158] Langer T, Förster D, Busse C, Michely T, Pfnür H and Tegenkamp C 2011 *New J. Phys.* **13** 053006
- [159] Dos Santos J L, Peres N and Neto A C 2007 *Phys. Rev. Lett.* **99** 256802
- [160] Shallcross S, Sharma S and Pankratov O A 2008 *Phys. Rev. Lett.* **101** 056803
- [161] Shallcross S, Sharma S, Kandelaki E and Pankratov O 2010 *Phys. Rev. B* **81** 165105
- [162] Trambly de Laissardière G, Mayou D and Magaud L 2010 *Nano Lett.* **10** 804–8
- [163] Mele E J 2010 *Phys. Rev. B* **81** 161405
- [164] Dos Santos J L, Peres N and Neto A C 2012 *Phys. Rev. B* **86** 155449
- [165] Trambly De Laissardière G, Mayou D and Magaud L 2012 *Phys. Rev. B* **86** 125413
- [166] Lu X *et al* 2019 *Nature* **574** 653–7
- [167] Polshyn H, Yankowitz M, Chen S, Zhang Y, Watanabe K, Taniguchi T, Dean C R and Young A F 2019 *Nat. Phys.* **15** 1011–6
- [168] Sharpe A L, Fox E J, Barnard A W, Finney J, Watanabe K, Taniguchi T, Kastner M and Goldhaber-Gordon D 2019 *Science* **365** 605–8
- [169] Serlin M, Tschirhart C, Polshyn H, Zhang Y, Zhu J, Watanabe K, Taniguchi T, Balents L and Young A 2020 *Science* **367** 900–3
- [170] Saito Y, Ge J, Watanabe K, Taniguchi T and Young A F 2020 *Nat. Phys.* **16** 926–30
- [171] Zondiner U *et al* 2020 *Nature* **582** 203–8
- [172] Wong D, Nuckolls K P, Oh M, Lian B, Xie Y, Jeon S, Watanabe K, Taniguchi T, Bernevig B A and Yazdani A 2020 *Nature* **582** 198–202
- [173] Stepanov P, Das I, Lu X, Fahimniya A, Watanabe K, Taniguchi T, Koppens F H, Lischner J, Levitov L and Efetov D K 2020 *Nature* **583** 375–8
- [174] Xu Y, Liu S, Rhodes D A, Watanabe K, Taniguchi T, Hone J, Elser V, Mak K F and Shan J 2020 *Nature* **587** 214–8
- [175] Rozen A *et al* 2021 *Nature* **592** 214–9
- [176] Cao Y, Rodan-Legrain D, Park J M, Yuan N F, Watanabe K, Taniguchi T, Fernandes R M, Fu L and Jarillo-Herrero P 2021 *Science* **372** 264–71
- [177] Stepanov P, Xie M, Taniguchi T, Watanabe K, Lu X, MacDonald A H, Bernevig B A and Efetov D K 2021 *Phys. Rev. Lett.* **127** 197701
- [178] Berdyugin A I *et al* 2022 *Science* **375** 430–3

- [179] Turkel S *et al* 2022 *Science* **376** 193–9
- [180] Yu K, Van Luan N, Kim T, Jeon J, Kim J, Moon P, Lee Y H and Choi E 2019 *Phys. Rev. B* **99** 241405
- [181] San-Jose P and Prada E 2013 *Phys. Rev. B* **88** 121408
- [182] Tsim B, Nam N N and Koshino M 2020 *Phys. Rev. B* **101** 125409
- [183] Moon P, Son Y W and Koshino M 2014 *Phys. Rev. B* **90** 155427
- [184] Zou X *et al* 2013 *Phys. Rev. Lett.* **110** 067401
- [185] Calderón M J and Bascones E 2020 *npj Quantum Mater.* **5** 57
- [186] Tabert C J and Nicol E J 2013 *Phys. Rev. B* **87** 121402
- [187] Havener R W, Liang Y, Brown L, Yang L and Park J 2014 *Nano Lett.* **14** 3353–7
- [188] Novelli P, Torre I, Koppens F H, Taddei F and Polini M 2020 *Phys. Rev. B* **102** 125403
- [189] Dai Z B, He Y and Li Z 2021 *Phys. Rev. B* **104** 045403
- [190] Moon P and Koshino M 2013 *Phys. Rev. B* **88** 241412
- [191] Natalin N, Kundelev E, Rukhlenko I D and Tepliakov N 2023 *Electron. Struct.* **5** 024008
- [192] Chang K, Zheng Z, Sipe J E and Cheng J L 2022 *Phys. Rev. B* **106** 1–11
- [193] Wang Y, Ni Z, Liu L, Liu Y, Cong C, Yu T, Wang X, Shen D and Shen Z 2010 *ACS Nano* **4** 4074–80
- [194] Vela A, Moutinho M, Culchac F, Venezuela P and Capaz R B 2018 *Phys. Rev. B* **98** 155135
- [195] Wang Y, Yu G, Rösner M, Katsnelson M I, Lin H Q and Yuan S 2021 *Phys. Rev. X* **12** 21055
- [196] Ochoa H and Asenjo-Garcia A 2020 *Phys. Rev. Lett.* **125** 37402
- [197] Lee H Y, Al Ezzi M M, Raghuvanshi N, Chung J Y, Watanabe K, Taniguchi T, Garaj S, Adam S and Gradecak S 2021 *Nano Lett.* **21** 2832–9
- [198] Zhao S *et al* 2021 *Nat. Commun.* **12** 6–12
- [199] Wu X, Fu C and Zhang Z M 2019 *Opt. Commun.* **452** 124–9
- [200] Qiao J, Kong X, Hu Z X, Yang F and Ji W 2014 *Nat. Commun.* **5** 4475
- [201] Li L *et al* 2017 *Nat. Nanotechnol.* **12** 21–25
- [202] Khaliji K, Martín-Moreno L, Avouris P, Oh S H and Low T 2022 *Phys. Rev. Lett.* **128** 193902
- [203] Lee S *et al* 2023 *Nat. Commun.* **14** 3889
- [204] Stauber T and Kohler H 2016 *Nano Lett.* **16** 6844–9
- [205] Lewandowski C and Levitov L 2019 *Proc. Natl Acad. Sci.* **116** 20869–74
- [206] Stauber T, Low T and Gómez-Santos G 2018 *Phys. Rev. Lett.* **120** 46801
- [207] Yin J, Wang H, Peng H, Tan Z, Liao L, Lin L, Sun X, Koh A L, Chen Y, Peng H and Liu Z 2016 *Nat. Commun.* **7** 10699
- [208] Patel H, Havener R W, Brown L, Liang Y, Yang L, Park J and Graham M W 2015 *Nano Lett.* **15** 5932–7
- [209] Ding C, Gao H, Sun L, Ma X and Zhao M 2021 *Phys. Rev. B* **104** 155427
- [210] Stern F 1967 *Phys. Rev. Lett.* **18** 546
- [211] Brey L, Stauber T, Slipchenko T and Martín-Moreno L 2020 *Phys. Rev. Lett.* **125** 256804
- [212] Zhou M 2021 *Phys. Rev. B* **104** 045419
- [213] Papaj M and Lewandowski C 2020 *Phys. Rev. Lett.* **125** 066801
- [214] Song J, Zhang Z, Feng N and Wang J 2021 *Nanomaterials* **11** 2433
- [215] Lin X, Liu Z, Stauber T, Gómez-Santos G, Gao F, Chen H, Zhang B and Low T 2020 *Phys. Rev. Lett.* **125** 077401
- [216] Stauber T, Low T and Gómez-Santos G 2020 *Nano Lett.* **20** 8711–8
- [217] Margetis D and Stauber T 2021 *Phys. Rev. B* **104** 115422
- [218] Ding C, Zhang X, Gao H, Ma X, Li Y and Zhao M 2022 *Phys. Rev. B* **106** 155402
- [219] Westerhout T, Katsnelson M I and Rösner M 2021 *2D Mater.* **9** 014004
- [220] Do T N, Shih P H and Gumbs G 2023 *J. Phys.: Condens. Matter* **35** 455703
- [221] Hu F, Das S R, Luan Y, Chung T F, Chen Y P and Fei Z 2017 *Phys. Rev. Lett.* **119** 247402
- [222] Huang T *et al* 2022 *Nature* **605** 63–68
- [223] Su X, Huang T, Zheng B, Wang J, Wang X, Yan S, Wang X and Shi Y 2022 *Nano Lett.* **22** 8975–82
- [224] Wu Z, Kuang X, Zhan Z and Yuan S 2021 *Phys. Rev. B* **104** 205104
- [225] Chakraborty A, Dutta D and Agarwal A 2022 *Phys. Rev. B* **106** 155422
- [226] Kuang X, Zhan Z and Yuan S 2022 *Phys. Rev. B* **105** 245415
- [227] Wang C, Xie Y, Ma J, Hu G, Xing Q, Huang S, Song C, Wang F, Lei Y and Zhang J *et al* 2023 *Nano Lett.* **23** 6907–13
- [228] Xiao Y M, Xu W, Peeters F M and Van Duppen B 2017 *Phys. Rev. B* **96** 085405–20
- [229] Yang J *et al* 2022 *Science* **375** 1295–9
- [230] Papaj M and Lewandowski C 2023 *Sci. Adv.* **9** eadg3262
- [231] Otteneder M, Hubmann S, Lu X, Kozlov D A, Golub L E, Watanabe K, Taniguchi T, Efetov D K and Ganichev S D 2020 *Nano Lett.* **20** 7152–8
- [232] Ikeda T N 2020 *Phys. Rev. Res.* **2** 032015
- [233] Herzig Sheinfux H and Koppens F H 2020 *Nano Lett.* **20** 6935–6
- [234] Topp G E, Jotzu G, McIver J W, Xian L, Rubio A and Sentef M A 2019 *Phys. Rev. Res.* **1** 023031
- [235] Du M, Liu C, Zeng Z and Li R 2021 *Phys. Rev. Res.* **104** 033113
- [236] Katz O, Refael G and Lindner N H 2020 *Phys. Rev. B* **102** 155123
- [237] Vogl M, Rodríguez-Vega M and Fiete G A 2020 *Phys. Rev. Res.* **101** 241408
- [238] Vogl M, Rodríguez-Vega M and Fiete G A 2020 *Phys. Rev. B* **101** 235411
- [239] Brihuega I, Mallet P, González-Herrero H, De Laissardière G T, Ugeda M, Magaud L, Gómez-Rodríguez J M, Ynduráin F and Veuille J Y 2012 *Phys. Rev. Lett.* **109** 196802
- [240] Zuber J W and Zhang C 2021 *Phys. Rev. B* **103** 245417
- [241] Yang F *et al* 2020 *Matter* **3** 1361–76
- [242] Du L, Dai Y and Sun Z 2020 *Matter* **3** 987–8
- [243] Di Mauro V L and Principi A 2022 *Phys. Rev. B* **106** 035401
- [244] Shimazaki Y, Yamamoto M, Borzenets I V, Watanabe K, Taniguchi T and Tarucha S 2015 *Nat. Phys.* **11** 1032–6
- [245] Gao Y, Zhang Y and Xiao D 2020 *Phys. Rev. Lett.* **124** 077401
- [246] Ha S *et al* 2021 *Light: Sci. Appl.* **10** 19
- [247] Hu J X, Xie Y M and Law K 2023 *Phys. Rev. B* **107** 075424
- [248] Molinero E B, Datta A, Calderón M J, Bascones E and Silva R E 2023 arXiv:2302.04127
- [249] Zhang S, Lu X and Liu J 2022 *Phys. Rev. Lett.* **128** 1–20
- [250] Kim B, Jin J, Wang Z, He L, Christensen T, Mele E J and Zhen B 2023 *Nat. Photon.* **18** 1–8
- [251] Stepanov E A, Semin S V, Woods C R, Vandelli M, Kimel A V, Novoselov K S and Katsnelson M I 2020 *ACS Appl. Mater. Interfaces* **12** 27758–64
- [252] Goodwin Z A, Corsetti F, Mostofi A A and Lischner J 2019 *Phys. Rev. B* **100** 235424
- [253] Gonzalez J and Stauber T 2019 *Phys. Rev. Lett.* **122** 26801
- [254] Cea T and Guinea F 2021 *Proc. Natl Acad. Sci.* **118** e2107874118
- [255] Sharma G, Trushin M, Sushkov O P, Vignale G and Adam S 2020 *Phys. Rev. Res.* **2** 022040
- [256] Lewandowski C, Chowdhury D and Ruhman J 2021 *Phys. Rev. B* **103** 235401
- [257] Törmä P, Peotta S and Bernevig B A 2022 *Nat. Rev. Phys.* **4** 528–42

- [258] Wu F, MacDonald A H and Martin I 2018 *Phys. Rev. Lett.* **121** 257001
- [259] Lian B, Wang Z and Bernevig B A 2019 *Phys. Rev. Lett.* **122** 257002
- [260] Peltonen T J, Ojajarvi R and Heikkilä T T 2018 *Phys. Rev. B* **98** 220504
- [261] Guinea F and Walet N R 2018 *Proc. Natl Acad. Sci. USA* **115** 13174–9
- [262] Cea T 2023 *Phys. Rev. B* **107** L041111
- [263] Cea T, Pantaleón P A, Walet N R and Guinea F 2022 *Nano Mater. Sci.* **4** 27–35
- [264] Peng L, Yudhistira I, Vignale G and Adam S 2023 arXiv:2309.14767
- [265] Martin I 2020 *Ann. Phys., NY* **417** 168118
- [266] Migdal A 1958 *Sov. Phys.-JETP* **7** 996–1001
- [267] Takada Y 1992 *J. Phys. Soc. Japan* **61** 3849–52
- [268] Uri A *et al* 2023 *Nature* **660** 1–6
- [269] Devakul T, Ledwith P J, Xia L Q, Uri A, de la Barrera S C, Jarillo-Herrero P and Fu L 2023 *Sci. Adv.* **9** eadi6063
- [270] Meng H, Zhan Z and Yuan S 2023 *Phys. Rev. B* **107** 035109
- [271] Cea T, Pantaleón P A and Guinea F 2020 *Phys. Rev. B* **102** 155136
- [272] Shi J, Zhu J and MacDonald A 2021 *Phys. Rev. B* **103** 075122
- [273] Long M, Pantaleón P A, Zhan Z, Guinea F, Silva-Guillén J A and Yuan S 2022 *npj Comput. Mater.* **8** 73
- [274] Long M, Zhan Z, Pantaleón P A, Silva-Guillén J A, Guinea F and Yuan S 2023 *Phys. Rev. B* **107** 115140
- [275] Fujimoto M, Kawakami T and Koshino M 2022 *Phys. Rev. Res.* **4** 043209
- [276] Song Z, Sun X and Wang L W 2021 *Phys. Rev. B* **103** 245206
- [277] Mullan C *et al* 2023 *Nature* **620** 1–6
- [278] Reidy K, Varnavides G, Thomsen J D, Kumar A, Pham T, Blackburn A M, Anikeeva P, Narang P, LeBeau J M and Ross F M 2021 *Nat. Commun.* **12** 1290
- [279] Li T *et al* 2021 *Nature* **600** 641–6
- [280] Li T *et al* 2021 *Nature* **597** 350–4
- [281] Uri A *et al* 2020 *Nature* **581** 47–52
- [282] Kazmierczak N P, Van Winkle M, Ophus C, Bustillo K C, Carr S, Brown H G, Ciston J, Taniguchi T, Watanabe K and Bediako D K 2021 *Nat. Mater.* **20** 956–63
- [283] Wilson J H, Fu Y, Sarma S D and Pixley J 2020 *Phys. Rev. Res.* **2** 023325
- [284] Namarvar O F, Missaoui A, Magaud L, Mayou D and de Laissardière G T 2020 *Phys. Rev. B* **101** 245407
- [285] Nakatsuji N and Koshino M 2022 *Phys. Rev. B* **105** 245408
- [286] Forsythe C, Zhou X, Watanabe K, Taniguchi T, Pasupathy A, Moon P, Koshino M, Kim P and Dean C R 2018 *Nat. Nanotechnol.* **13** 566–71